Chemical Evolution of Pt–Zn Nanoalloys Dressed in Oleylamine

Alter Zakhtser, Ahmed Naitabdi, Rabah Benbalagh, François Rochet, Caroline Salzemann, Christophe Petit, Suzanne Giorgio

To cite this version:

Alter Zakhtser, Ahmed Naitabdi, Rabah Benbalagh, François Rochet, Caroline Salzemann, et al.. Chemical Evolution of Pt–Zn Nanoalloys Dressed in Oleylamine. ACS Nano, 2021, 15 (3), pp.4018-4033. 10.1021/acsnano.0c03366 . hal-03943210

HAL Id: hal-03943210
https://hal.science/hal-03943210

Submitted on 1 Feb 2023

Chemical Evolution of Pt-Zn Nanoalloys Dressed in Oleylamine

Alter Zakhtser[1,2], *Ahmed Naitabdi*[2*], *Rabah Benbalagh,*[2] *François Rochet*[2*], *Caroline Salzemann*[1*], *Christophe Petit*[1], *Suzanne Giorgio*[3]

[1]Sorbonne Université, CNRS, MONARIS, UMR 8233, 4 place Jussieu, 75005 Paris, France.

[2]Sorbonne Université, CNRS, LCPMR, UMR 7614, 4 place Jussieu, 75005 Paris, France

[3]Aix Marseille Université, CNRS, CINaM, UMR 7325, 13288 Marseille, France

CORRESPONDING AUTHORS

Ahmed Naitabdi E-mail : ahmed.nait_abdi@sorbonne-universite.fr; Caroline Salzemann E-mail : caroline.salzemann@sorbonne-universite.fr; François Rochet E-mail : francois.rochet@sorbonne-universite.fr;

KEYWORDS: Bimetallic catalysts, platinum, zinc, ageing, oxidation, zinc leaching, oleylamine, transmission electron microscopy, monochromatic x-ray photoemission spectroscopy.

ABSTRACT: We report on the shape, composition (from $Pt_{95}Zn_5$ to $Pt_{77}Zn_{23}$) and surface chemistry of Pt-Zn nanoparticles obtained by reduction of precursors $M^{2+}(acac)_2^-$ (M^{2+}: Pt^{2+} and

Zn^{2+}) in oleylamine, which serves as both solvent and ligand. We show first that the addition of phenyl ether or benzyl ether determines the composition and shape of the nanoparticles, which point to an adsorbate-controlled synthesis. The organic (ligand)/ inorganic (nanoparticles) interface is characterized on the structural and chemical level. We observe that the particles, after washing with ethanol, are coated with oleylamine and the oxidation products of the latter, namely an aldimine and a nitrile. After exposure to air, the particles oxidize covering themselves with a few monolayer thick ZnO film, which is certainly discontinuous when the particles are low in zinc. Pt-Zn particles are unstable and prone to losing Zn. We have strong indications that the driving force is the preferential oxidation of the less noble metal. Finally, we show that adsorption of CO on the surface of nanoparticles modifies the oxidation state of amine ligands and attribute it to the displacement of hydrogen adsorbed on Pt. All the structural and chemical information provided by the combination of electron microscopy and X-ray photoelectron spectroscopy allows us to give a fairly accurate picture of the surface of nanoparticles and to better understand why Pt-Zn alloys are efficient in certain electrocatalytic reactions such as the oxidation of methanol.

Platinum plays a prominent role in heterogeneous catalysis, especially in the dehydrogenation of alkanes,[1] and in CO oxidation[2–4] However, its combination with oxides emerged quickly as a key solution to alleviate the cost of this precious metal and to increase its efficiency.[5,6] Limiting ourselves to the case of CO oxidation, ultrathin oxide islands of 3d transition metal covering partly a platinum surface appeared very efficient to circumvent the issue of CO surface poisoning[7] at low temperature, as CO is oxidized at the contact line[8] between Pt and the transition metal oxide. This type of mechanism falls into the more general category of inverse oxide/metal catalysts, as defined by Jan Hrbek and J.A. Rodriguez.[6,9] Besides nickel or iron oxides,[10,11] zinc oxide has emerged as an effective co-catalyst on Pt surfaces at low temperature.[9,12] Using near-ambient X-ray photoemission spectroscopy to examine *in situ* the oxidation of CO on the ZnO/Pt(111) surface, we have recently demonstrated the presence of carboxyls resulting from the association of CO with hydroxyls provided by the zinc oxide islands at the phase boundary and highlighted their role in the oxidation mechanism.[9]

Platinum is also a prominent element in electrocatalysis, particularly in the context of the development of polymer electrolyte membrane fuel cells. Platinum supported on carbon is generally used as the catalyst *both* for the anode (where the hydrogen oxidation reaction takes place) and the cathode (where the oxygen reduction reaction or ORR occurs). Despite being the most active element for ORR, the reaction remains sluggish, and the combination of Pt with partly filled 3d band transition metals was actively studied. In electrocatalysis, alloying is thought to modify the energy position of the d-band of platinum, through charge transfer from the less-noble metal, or through strain effects on the platinum lattice (after the less-noble metal has left the surface), so as to modulate the adsorption energies of the molecules, active or spectator in the surface chemical reaction.[13,14] The formation of a “Pt skin” over a Pt_3Ni alloy seems to be the key point to explain a catalytic enhancement in ORR four times higher than for pure Pt.[15] The so-called bifunctional mechanism is an alternative option. Considering Pt alloyed with a less-noble metal *M*, more oxophilic than Pt, *M* will capture an OH from the electrolyte that will then react with a CO molecule adsorbed on a nearby platinum. This OH-spillover mechanism is well-documented for Pt−Ru anodes in direct methanol fuel cells.[13] This view adopted in electrocatalysis is finally similar to that of inverse oxide/metal catalysis. Regarding alloying of platinum with zinc, bimetallic nanoparticles (PtZn and Pt_3Zn intermetallics) have a proven efficiency for ORR,[16] but their use has attracted most attention for the oxidation reaction of formic acid (FAOR) and that of methanol (MOR).[13] In particular Pt_3Zn catalysts are remarkably resistant to poisoning by CO and other carbonaceous species produced during the MOR process.[17] The reason why this happens remains largely elusive.

The present study is devoted to the morphology and chemistry of Pt-Zn alloy nanoparticles, grown at high temperature (350°C) in an oleylamine solution, from platinum bis(acetylacetonato)platinum(II) ($Pt(acac)_2$) and bis(acetylacetonato)zinc(II) ($Zn(acac)_2$) precursors (the respective molecules are depicted in Figure 1). Oleylamine plays here a triple role, as a solvent, a reducing agent and a ligand (a stabilizer). Oleylamine and ether additives are also used to control the particle shapes. The growth method, a variant of that proposed by Kang *et al.*,[17] enables the production of bimetallic alloy particles with a wider compositional range (from $Pt_{77}Zn_{23}$ to $Pt_{95}Zn_5$) than in the preceding work. The synthesis also differs from another method proposed more recently using the so-called "underpotential deposition" strategy together with weak reduction conditions, *in the absence of amine surfactants.*[18]

In the present study we devote as much attention to the oleylamine capping as to the bimetallic particle itself, because the organic shell is known to play a crucial role in reactivity,[19] in particular as a selectivity switcher.[20] The produced nanoparticles are studied as synthesized, with their oleylamine shell. Although annealing at 600°C in air would stabilize the ordered intermetallic phase Pt_3Zn,[17] it would mean the destruction of the oleylamine shell, especially important in homogeneous catalysis with colloids, and thus reduce the extent of information collected.

The question of the morphology and chemical composition of the grown nanoparticles is examined in detail. Indeed, previous works[13] have clearly shown that compositional variations in the nanoalloy, between its surface and core, have a significant impact on reactivity. Shape also matters. Indeed, the orientation of the facets displayed by the nanoparticles plays a major role in electrocatalysis. Taking the ORR as an example, the predominant crystallographic planes at the surface of *shape-controlled* Pt particles are responsible for their different catalytic activity.[21]

Therefore, if an electrocatalytic application of Pt-Zn nanocatalysts is in the line of sight, the shape control is of prime importance. This control can be achieved by choosing the right additives[22] that may or may not block the growth of a given facet. For instance, Kang and coworkers demonstrated that benzyl ether in pure oleylamine induces a change in the morphology of nanoparticles from quasi-spherical (in its absence) to cubic (in its presence).[17] Using variations in the nanoparticle growth process with respect to the procedure defined in Ref.[17], we have determined by transmission electron microscopy (TEM) and energy-dispersive X-ray spectroscopy (EDX), combined with scanning electron microscopy (SEM), the shape and composition changes related to the use of two different ether additives (benzyl ether versus phenyl ether).

The second, but related aspect that is tackled thoroughly in this work, is the nature of the chemical bonding. X-ray photoelectron spectroscopy gave us crucial information on the oxidation state of the metals and of the oleylamine ligand (*i.e.* its dehydrogenation state) that escapes to electron microscopy, which makes the combination of both tools highly valuable. Then, we have examined the chemical stability of the ensemble “bimetallic nanoparticle and amine ligand”. We have followed the leaching of less-noble metal, zinc, due to its slow oxidation in toluene, and established correlations with our TEM observations. This is clearly related to the issue of nanoparticle activation in electrocatalysis and the formation of the “Pt skin”.[13] We have also examined the chemistry of the metal/oleylamine interface, by a mild thermal annealing (400 K) in ultra-high vacuum or by exposure to CO/O_2 mixtures at room temperatures. As these treatments affect the chemistry of the oleylamine head, our findings shed new light on the surface chemistry of the dressed metallic particles, with implications both on particle growth and reactivity.

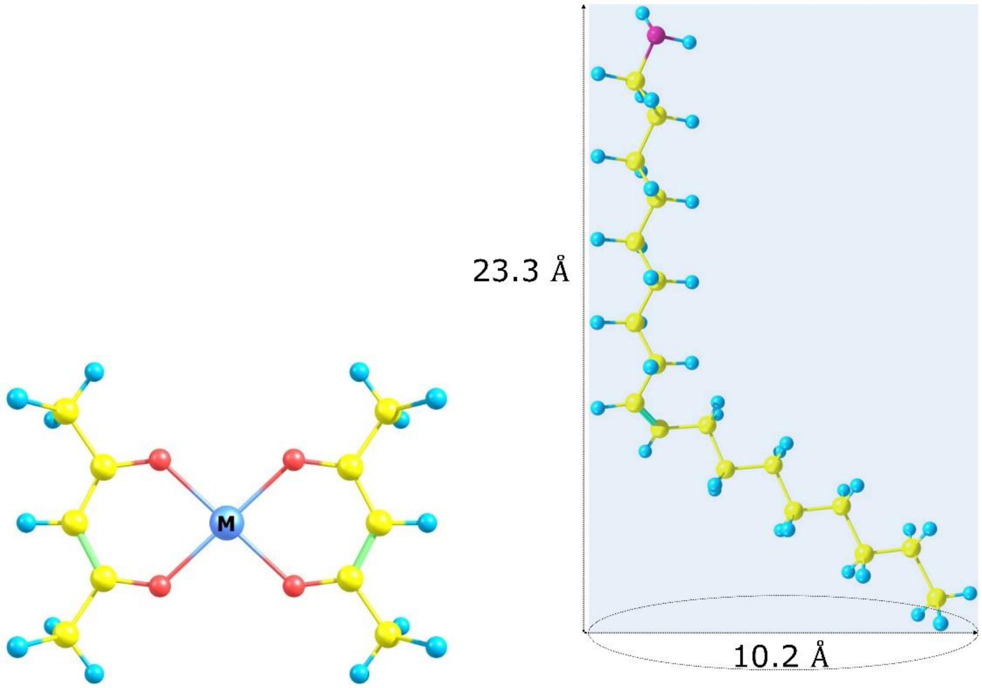

Figure 1. (left) The M^{2+} (Pt^{2+} or Zn^{2+}) bis(acetylacetonate) $(acac^{-})_2$ precursors. (right) the oleylamine solvent. Carbon, oxygen, nitrogen and hydrogen atoms are in yellow, red, violet and turquoise, respectively.

RESULTS AND DISCUSSION

Structural and chemical characterization of "fresh" particles

Particles with compositions $Pt_{95}Zn_5$, $Pt_{86}Zn_{14}$ and $Pt_{77}Zn_{23}$, (see Table 1) were characterized by a combination of TEM (Figure 2), HRTEM (Figure 3) and monochromatized XPS (Al K_α 1486.7 eV) (Figures 4 and 5) to gain both structural and chemical information. As we shall see it later, the time of storage in toluene has a huge impact on the chemistry of the nanoparticles, therefore the ageing time in this solvent is always indicated. The qualifier "fresh" means that the storage time does not exceed one day. Note that before examination by microscopy or XPS, the samples are inevitably exposed to air during transfer.

The TEM micrograph of Figure 2 (a-c) shows "fresh" $Pt_{95}Zn_5$ and $Pt_{86}Zn_{14}$ particles prepared in the presence of the benzyl ether additive. These are cuboids displaying {100} faces, with average sizes of ~11 nm (a), ~8 nm (b) and ~5 nm (c). The observed shape is that expected, as it has been shown by Kang *et al.*[17] that the addition of benzyl ether in pure oleylamine favors the cuboidal geometry. The average "edge-to-edge distance", or "organic gap", separating the metallic surfaces ranges from ~2.1 nm (~11 nm wide $Pt_{95}Zn_5$) to 2.6 nm (~5 nm wide $Pt_{86}Zn_5$).

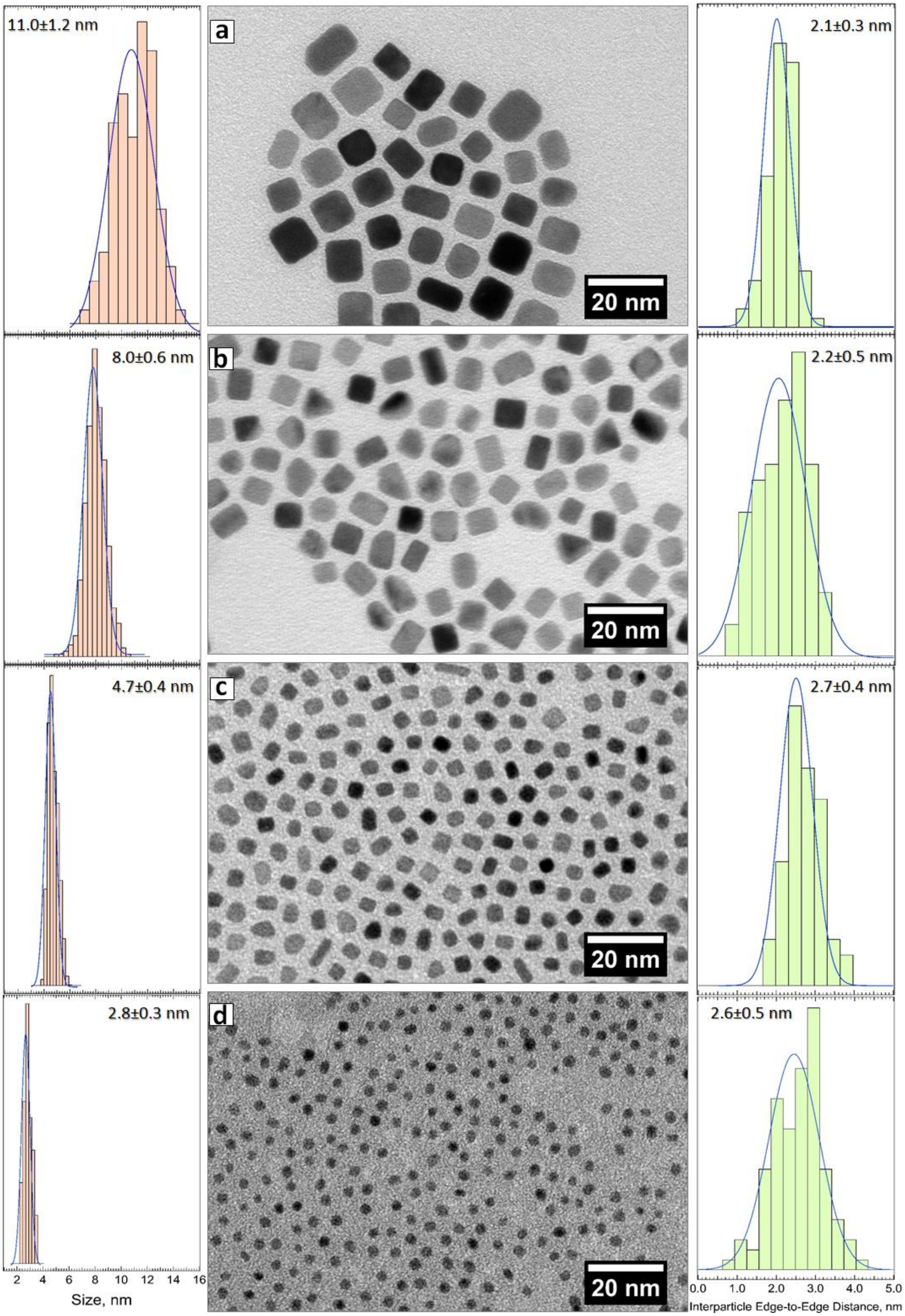
11.0±1.2 nm
a
20 nm
2.1±0.3 nm
8.0±0.6 nm
b
20 nm
2.2±0.5 nm
4.7±0.4 nm
c
20 nm
2.7±0.4 nm
2.8±0.3 nm
d
20 nm
2.6±0.5 nm
2
4
6
8
10
12
14
16
Size, nm
0.0
1.0
2.0
3.0
4.0
5.0
Interparticle Edge-to-Edge Distance, nm

Figure 2. Center: TEM micrographs PtZn nanoparticles synthesized in oleylamine from $Pt(acac)_2$ and $Zn(acac)_2$ precursors at 350°C (see Table 1): (a) fresh ~11 nm wide cuboidal $Pt_{95}Zn_5$ nanoparticles grown in the presence of benzyl ether (argon purified oleylamine), (b) fresh ~8 nm wide cuboidal $Pt_{86}Zn_{14}$ nanoparticles grown in the presence of benzyl ether (argon purified oleylamine), (c) fresh ~5 nm cuboidal $Pt_{86}Zn_{14}$ grown in the presence of benzyl ether (no Ar bubbling), (d) fresh ~2.8 nm wide $Pt_{77}Zn_{23}$ nanoparticles grown in the presence of phenylether. The size distribution (diameter) is given in the left panel. The interparticle edge-to-edge distance (the "organic" gap between nanoparticles) is given in the right panel. The JEOL1011 microscope was operated at 100 kV.

The edge-to-edge length compares with the length of the oleylamine tail, ~2.5 nm (Figure 1). As the organic gap is less than twice the molecule length, there is only one monomolecular oleylamine outer shell around the particles, and in between the nanoparticles, the oleylamine shells are likely interdigitated. This was already reported for self-assemblies of capped metallic nanoparticles.[23,24]

Keeping the same ratio of precursors and growth temperature, but switching to the phenyl ether additive, the morphology and composition of the nanoparticles change drastically, as shown in Figure 2 (d). The "fresh" particles are now smaller (average size ~2.8 nm) and spherical. The 2.5 nm average inter-particle edge-to-edge distance (like that of the cuboids) indicates that the particles are dressed in one oleylamine shell. The observed spherical shape means that conversely to benzyl ether, the phenyl ether doesn't selectively adsorbed on {100} planes.. EDX shows also that the stoichiometry is $Pt_{77}Zn_{23}$, close to that of the intermetallic ordered alloy Pt_3Zn.

The HRTEM images of Figure 3 give valuable information on the nature of Pt-Zn alloy. The Fourier transform of the individual crystals gives two reflections labeled 1 and 2, corresponding, respectively, to the characteristic{002} (0.20±0.005 nm) and {011} (0.270.005 nm) reflections of ordered Pt_3Zn.[17] The {111} (0.225nm) reflection common to both pure platinum[25] and Pt_3Zn, is also found. Finally, we find no indication of zinc oxide nanoparticles (that were obtained when $Zn(acac)_2$ was only present). The observed particles are all metallic.

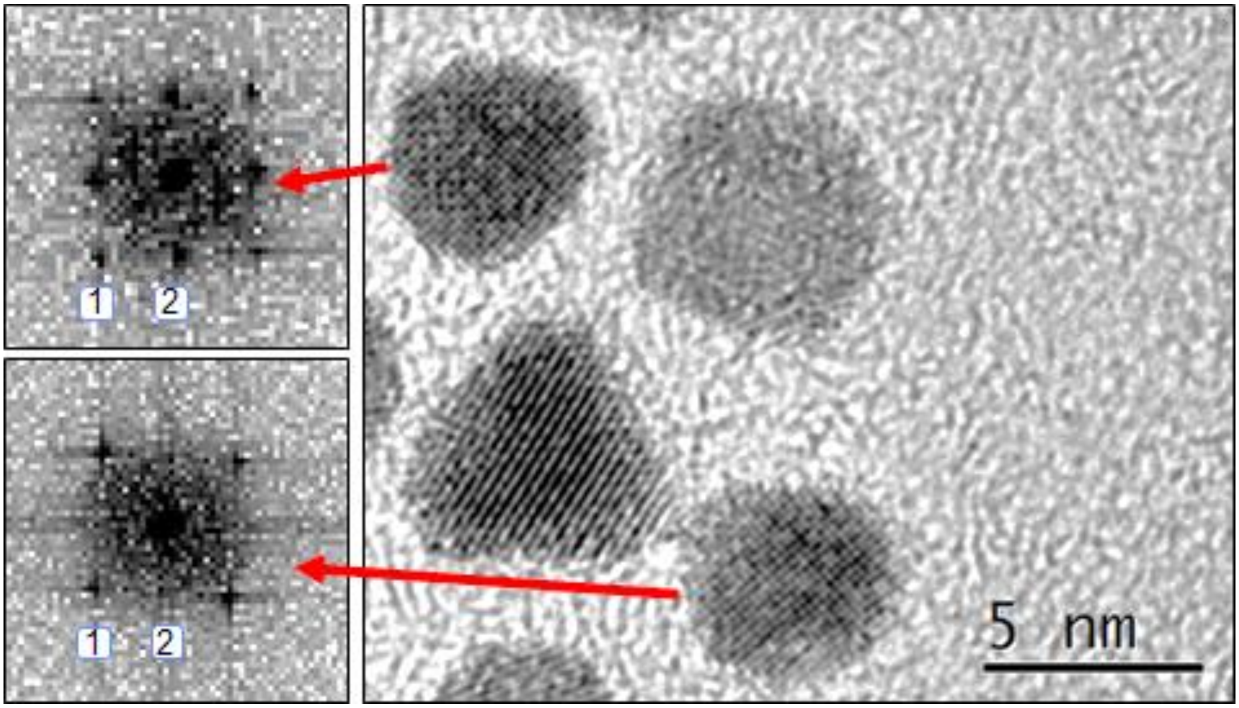

Figure 3. HRTEM image of fresh $Pt_{86}Zn_{14}$ particles. The Fourier transform gives two reflections labeled 1 and 2, corresponding to the {002} (0.20±0.03 nm) and {011} distances (0.27±0.03 nm), which are characteristic reflections of ordered Pt_3Zn. The JEOL JEM 2010A was operated at 200 kV.

Selected area electron diffraction (SAED) patterns of "fresh $Pt_{86}Zn_{14}$" (shown in Figure S4 of SI) agree with HRTEM concerning the formation of an alloy. The ~0.28 nm {011} interplanar distance of ordered Pt_3Zn is also clearly observed. The intermetallic is made at 350°C, although, according to Kang *et al.* the fully ordered, $AuCu_3$-type, alloy is normally produced after an annealing in air at 600°C.[17]

The SAED patterns also exhibit very faint diffraction rings corresponding to interplanar distances of 0.26±0.01 nm and 0.16±0.01 nm, found for zinc oxides.[26] These diffraction rings are observed only after long acquisition times, and thus the oxide content should be small. As HRTEM shows no ZnO particles in the fresh samples, we can speculate that ZnO is the result of the surface oxidation of the Pt-Zn particles during their exposure to air, prior to examination.

Microscopy analyses have given valuable insights on the structure and composition of the nanoparticles that we can now summarize. First, we obtain a Pt-Zn alloy and not a mixture of Pt and ZnO nanocrystals. Kang *et al.*[17] already noticed that obtaining the alloy is not self-evident, given the propensity of zinc to oxidize. The latter authors attributed the reduction of Zn^{2+} to Zn^0 to the high temperature involved in the process, without further explanation. All works[17,18] dealing with Pt-Zn growth (including the present one) concur in noting that the presence of the platinum precursor is crucial to avoid zinc oxide particle formation. Therefore, thermodynamics may favor the reduction of Zn^{2+} ions from $Zn(acac)_2$ molecules in the vicinity of a platinum facet, and its sticking on it, to the formation of zinc aggregates that will be then oxidized. Second, we find indications of the Pt_3Zn intermetallic compound in particles of average composition $Pt_{86}Zn_{14}$. This is suggestive of a zinc composition gradient in the particle. Third, we find that the ether additive has a strong influence both on shape (in agreement with the previous work[17]) and composition (this is new), as discussed below. In the presence of benzyl ether, {100} planes are observed, and particles are on average much richer in Pt than the Pt_3Zn stoichiometry. On the other hand, phenyl ether leads to spheres (cuboctahedra are formed) with an average composition very close to Pt_3Zn.

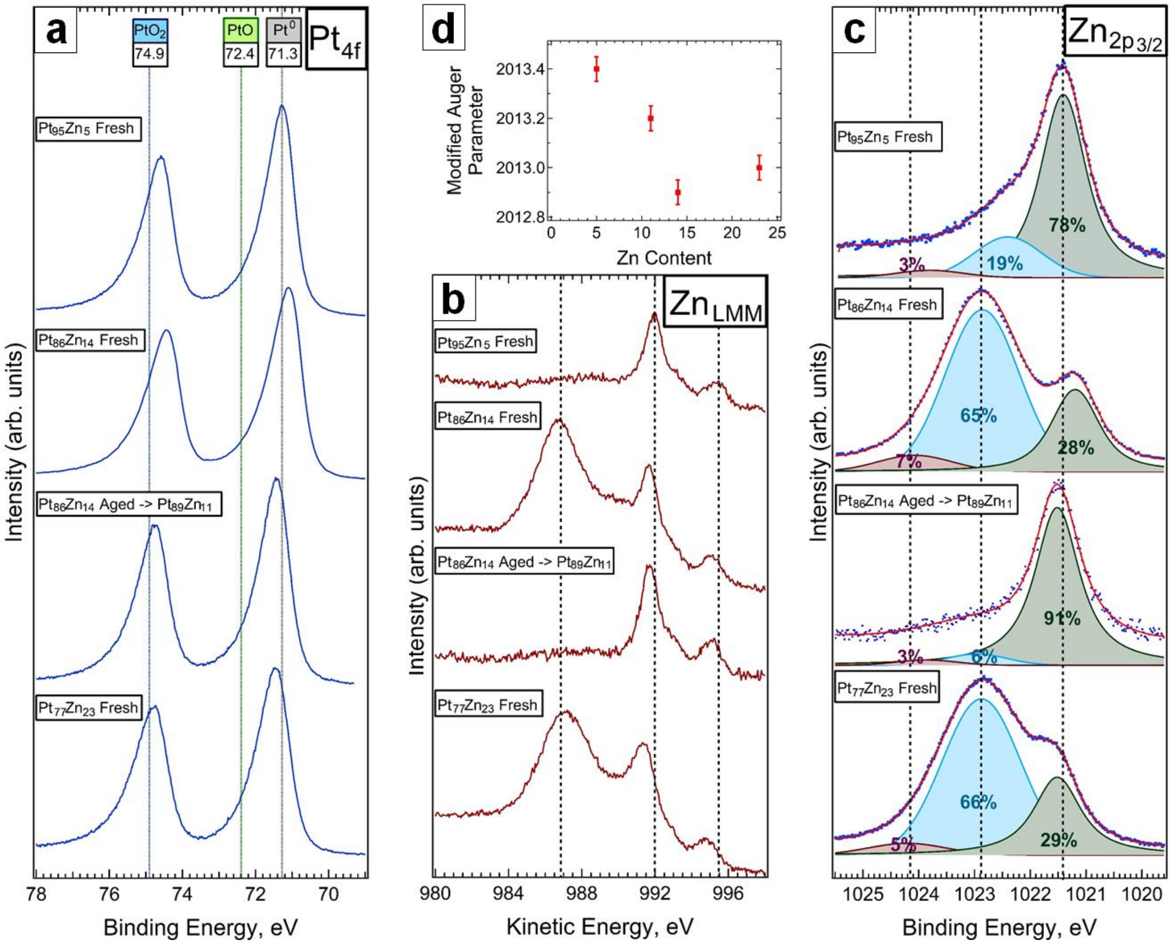

Figure 4. (a) Pt 4f, (b) $L_3M_{4,5}$ $M_{4,5}$ Zn Auger and (c) Zn $2p_{3/2}$ spectra of Pt_xZn_y nanoparticles. In panel (d) we give the modified Auger parameter α' versus Zn content (%) for metallic Zn. The photon energy is 1486.7 eV (monochromatized Al K_α source). The overall energy resolution is better than 640 meV. The binding and kinetic energy scales are not corrected.

We discuss now the XPS spectra that provide information on the chemical bonding of the metallic elements and on the organic dressing of the particles. The XPS experiments were carried out in identical conditions (geometry, photon flux *etc.*), with deposits a few µm thick. The films are expected to have a low conductivity because of the particle edge-to-edge distance (2.0 to 2.7 nm) and because oleylamine has a coupling constant of ~10 nm^{-1}. Thus, grounding the samples may be insufficient to compensate the positive charge created by the photoemission process. The phenomenon may be also aggravated using monochromatic excitation, for which the level of stray electrons in the chamber is low. However, only small charging effects,[27,29] less than 0.3 eV, were observed, depending on the samples. Therefore, all XPS spectra are plotted without binding energy corrections.

Let us now consider the metal core-level and Auger spectra, Pt 4f, Zn $L_3M_{4,5}M_{4,5}$ and Zn $2p_{3/2}$, of fresh nanoparticles. The Pt 4f spectra (Figure 4 (a)) of the "fresh" $Pt_{95}Zn_5$, $Pt_{86}Zn_{14}$ and $Pt_{77}Zn_{23}$ samples have identical shapes. The slight shifts in binding energy from one sample to another are not chemically meaningful, being due to a small charging effect. The Pt $4f_{7/2}$ peak maximum comprised between 71.1 eV and 71.4 eV point to platinum in a metallic state. Indeed, the Pt $4f_{7/2}$ binding energy of bulk platinum is reported between 71.1 eV and 71.3.[16] Considering that the Pt $4f_{7/2}$ full width at half maximum (FWHM) is 1.00±0.07 eV for all three samples, from the zinc-poor $Pt_{95}Zn_5$ to the zinc-rich $Pt_{77}Zn_{23}$, we find no indication of any alloying effect with Zn in the spectral shape, although an energy shift of +0.4 eV was reported when a Pt-Zn alloy forms at the surface of Pt crystal.[28] The $4f_{7/2}$ positions for PtO and PtO_2 are indicated by dashed vertical lines. We do not see any clear evidence of the presence of these oxides, whose precise quantitative determination remains difficult due to the asymmetric Doniach-Šunjić spectral shape of metallic platinum.

The Zn $L_3M_{4,5}M_{4,5}$ Auger (Figure 4 (b)) is generally used to distinguish Zn^{2+} from Zn^0 because of a much larger chemical shift than in the Zn 2p spectrum. For the Zn-poor 11 nm $Pt_{95}Zn_5$ particles, the Auger spectrum is essentially characteristic of metallic zinc (Zn^0) with its two multiplet structures $^1G_4$ at ~992 eV and $^3F_{2,3,4}$ at ~995 eV.[29] There is a weak "bump" at ~987 eV at the position of the $^1G_4$ multiplet of Zn^{2+}. In contrast, the Zn $L_3M_{4,5}M_{4,5}$ spectra of the 5 nm $Pt_{86}Zn_{14}$ and 2.8 nm $Pt_{77}Zn_{23}$ samples show that one part of the zinc atoms is oxidized (Zn^{2+}), as an intense $^1G_4$ component appears at a kinetic energy of ~987 eV, while the other part remains metallic with the $^1G_4$ and $^3F_{2,3,4}$ multiplets at 991.8 and 994.8 eV.

The Zn $2p_{3/2}$ photoelectron spectra of the fresh samples (Figure 4 (c)) all exhibit two components. The lower binding energy one, in the 1021.2-1021.6 eV range is attributed to metallic zinc Zn^0.[30,31] Considering the kinetic energy of the $^1G_4$ multiplet peak maximum and binding energy the Zn $2p_{3/2}$ peak maximum, we can form the modified Auger parameter α' that is the sum of both.[32,33] Being the difference of two kinetic energies, α' is not affected by charging effects.[27] As seen in Figure 4 (d), α' depends clearly on the average zinc content, as it ranges from 2013.4 eV for the $Pt_{95}Zn_5$ zinc-poor particles to 2012.9 eV for the $Pt_{86}Zn_{14}$ particles, in which Pt_3Zn is identified by HRTEM and SAED, and for the $Pt_{77}Zn_{23}$ ones. Thus α' is a good proxy to identify zinc leaching in the particles (see below).

A second component is seen in the Zn $2p_{3/2}$ spectra, at higher binding energy than that of Zn^0, in the 1022.5-1022.8 eV range. Its intensity correlates with that of the Zn^{2+} $^1G_4$ multiplet in the Auger spectrum, and therefore, we are inclined to attribute it to oxidized zinc. The Zn $2p_{3/2}$ binding energy values of zinc oxide have a considerable spread in the literature, from 1021.8 eV[34] (*i.e.* nearly identical to that of Zn metal) to 1022.3 eV in a wurtzite ZnO (0001) single crystal.[35] The binding energy shift between Zn^{2+} and Zn^0, $\Delta_{Zn^0}^{Zn^{2+}}$, goes from 1 eV for $Pt_{95}Zn_5$, to 1.2 eV for $Pt_{77}Zn_{23}$ and finally to 1.5 eV for $Pt_{86}Zn_{14}$. Such $\Delta_{Zn^0}^{Zn^{2+}}$ values were reported in the literature. For instance, in the case of an oxidized Zn-deposited/Cu(111) surface, the oxidized zinc component is found at ~1 eV from that of metallic Zn in the surface alloy.[36] To eliminate possible differential charging effects between the zinc oxide and the metallic particle (zinc oxide could make loose electrical contacts with the metallic particle), we have measured the Zn $2p_{3/2}$ spectra of $Pt_{86}Zn_{14}$ aged for 1 year particles in the presence of a flood gun. The spectra are shown and discussed in

Figure S5 of the SI. The spectral shape is not much affected by electron flooding, which shows that zinc oxide and metallic parts are in good electrical contact.[27] Therefore the image of a surface-oxidized nanoalloy (the oxide is ZnO) emerges further strengthened from our analysis. $\Delta_{\mathrm{Zn}^0}^{\mathrm{Zn}^{2+}}$ values around 1 eV can be explained by assuming that the Fermi level in the oxide (the gap of ZnO is 3.37 eV[37]) is close to the conduction band.[38]

We now turn our attention to the lowest binding energy component the O 1s spectrum (Figure 5(a)), in the range 531.1-531.5 eV. This component is attributed to zinc oxide at Pt-Zn particles (oxide@Pt-Zn). Indeed, the binding energy difference $\Delta_{\mathrm{O}\,1s}^{\mathrm{Zn}\,2p_{3/2}}(\text{oxide@Pt-Zn}) = \mathrm{Zn}\ 2p_{3/2}\ (\text{oxide@Pt-Zn}) - \mathrm{O}\ 1s\ (\text{oxide@Pt-Zn})$ ranges from 491.1 eV ($Pt_{95}Zn_5$) to 491.4 eV ($Pt_{86}Zn_{14}$ and $Pt_{77}Zn_{23}$). For bulk wurtzite, Fidelis *et al.*[35] find $\Delta_{\mathrm{O}\,1s}^{\mathrm{Zn}\,2p}(\text{wurtzite}) = 491.3$ eV. We find the same energy difference considering the wurtzite ZnO particles we have produced (see SI, section S1). The energy distance is smaller for thin *h*-BN-like ZnO films on Au(111) (*h*-BN-ZnO@Au(111)), as $\Delta_{\mathrm{O}\,1s}^{\mathrm{Zn}\,2p_{3/2}}(h\text{-BN-ZnO@Au(111)}) = 490.9$ eV. Therefore $\Delta_{\mathrm{O}\,1s}^{\mathrm{Zn}\,2p_{3/2}}$ may be a valuable "proxy" of the zinc oxide electronic structure. Note that the transition from *h*-BN-ZnO on Pt(111) to wurtzite-ZnO occurs for thicknesses greater than 4 monolayers (~0.85 nm).[39] Therefore, estimating the thickness of the oxide layer is of great help for the discussion.

From the Zn^{2+}: Zn^0 intensity distribution $\mathrm{I_{ZnO}}$: $\mathrm{I_{Zn(metal)}}$ measured from the Zn $2p_{3/2}$ core-level spectra, we can estimate the oxide thicknesses $\mathrm{d_{ZnO}}$ and the oxide surface fraction η_{ZnO} ($0<\eta_{\mathrm{ZnO}}<1$) considering that the oxide film may be discontinuous, leaving open Pt areas. First to simplify the calculation, we assume that ZnO caps a *flat*, semi-infinite metallic alloy. This approximation is more realistic for the big nanoparticles (cuboidal 5 to 11 nm wide particles) that for the smaller ones (spherical 2.8 nm wide particles), given the calculated inelastic mean free paths (IMFP) in Pt and ZnO of Table 2. Second, we assume that zinc is evenly distributed with increasing depth in the alloy. This may be not always exact, especially when zinc-leaching occurs (see below), but the composition provided by EDX, the only parameter at hand, averages out the gradients. The number of zinc atoms per unit volume $\mathrm{N}_{\mathrm{Zn}}^{\mathrm{ZnO}}$ is that of wurtzite (4.15×10^{22} atoms/cm^{3}). The number of zinc atoms per unit volume in Pt-Zn alloys $\mathrm{N}_{\mathrm{Zn}}^{\text{Pt-Zn}}$ is approximated by the number of Pt atoms per unit volume (6.62×10^{22} atoms/cm^{3}) multiplied by the zinc concentration provided by EDX. Therefore $\mathrm{I}_{\mathrm{ZnO}}/\mathrm{I}_{\mathrm{Zn(metal)}}$ can be written as:

$$\frac{\mathrm{I}_{\mathrm{ZnO}}}{\mathrm{I}_{\mathrm{Zn(metal)}}} = \frac{\mathrm{N}_{\mathrm{Zn}}^{\mathrm{ZnO}}\lambda_{\mathrm{ZnO}}\left(\exp\left(\frac{\mathrm{d}_{\mathrm{ZnO}}}{\lambda_{ZnO}}\right)-1\right)}{\mathrm{N}_{\mathrm{Zn}}^{\text{Pt-Zn}}\lambda_{\text{Pt-Zn}}\left(1+\left(\frac{1-\eta_{\mathrm{ZnO}}}{\eta_{\mathrm{ZnO}}}\right)\exp\left(\frac{\mathrm{d}_{\mathrm{ZnO}}}{\lambda_{ZnO}}\right)\right)} \quad [1]$$

Where λ_{ZnO} and $\lambda_{\text{Pt-Zn}}$ are the IMFP in ZnO and the Pt-Zn alloy respectively ($\lambda_{\text{Pt-Zn}}$ is approximated by the IMFP in bulk Pt, λ_{Pt}). The IMFP values are collected in Table 2.

If we assume a continuous film ($\eta_{\mathrm{ZnO}} = 1$ in [1]), then we can calculate an equivalent thickness of 0.02 nm for the 11 nm wide $Pt_{95}Zn_{5}$ particles. This value is unrealistically thin. Taking into consideration the low $\Delta_{\mathrm{O}\ 1s}^{\mathrm{Zn}\ 2p_{3/2}}$ value,[35] the fresh $Pt_{95}Zn_{5}$ particles may be covered by a few *h*-BN like ZnO layers of thickness ~0.22 nm each. Therefore, the calculated fraction η_{ZnO} of the surface covered by mono- (0.22 nm) , bi- (0.44 nm) and tri-layers (0.66 nm) of ZnO is 9.4%, 5.1%, and 3.7% respectively, suggesting that most of the surface of the particle is platinum.

If we consider now the 5 nm wide $Pt_{86}Zn_{14}$ and 2.8 nm wide $Pt_{77}Zn_{23}$ nanoparticles, taking η_{ZnO} equal to 1, we find equivalent ZnO thicknesses of 0.40 nm and 0.55 nm. This corresponds to 2 to 3 *h*-BN like ZnO layers. Therefore, the equivalent thicknesses are compatible with the hypothesis of a continuous film. However the $\Delta_{\mathrm{O}\ 1s}^{\mathrm{Zn}\ 2p_{3/2}}$ parameter being that of wurtzite,[35] and considering that the transition from *h*-BN like ZnO to wurtzite occurs above 4 layers,[39] we must consider the hypothesis of a discontinuous film, locally thicker than the equivalent thickness.

Using equation [1] we find that 49% (65%) of the $Pt_{86}Zn_{14}$ ($Pt_{77}Zn_{23}$) particle surface is covered by ZnO when a 5-layer oxide (1.1 nm) is considered.

While TEM cannot provide information on the oleylamine dressing due to the low Z of the C, N and O elements, XPS sheds light on the chemical bonding of the organic part by exploiting the characteristic binding energies and chemical shifts. The C 1s spectrum is not very informative as it is dominated by the contribution of the (mainly aliphatic) carbons of the oleylamine “tail”. The components between 532.5 eV and 533.5 eV in the O 1s spectra (Figure 5(a)) could be related to organic species involved in the preparation (acac, ethers) trapped in the organic shell, or to contaminants adsorbed on the particles after exposure in air. Concerning $acac^-$ and Hacac, the aliphatic carbonyls should be found at 532.3 eV.[40] Benzyl ether O 1s is expected at 532.6 eV, and phenyl ether O 1s at 533.2 eV.[40] Carboxylic acid that are ubiquitous contaminants have components at 532.2 and 533.6 eV.[40] They may adsorb on the sample after exposure to air.

The N 1s spectra (Figure 5(b)) of the amine head give crucial information on the chemical state of the ligand amine head. The N 1s spectra of the “fresh” samples are all very similar. All spectra are fitted with four components at 401 eV, 399.7 eV, 398.4 eV and 397.4 eV. Using the flood gun (30 V, 10 μA) we have verified that the binding energy shifts of these components are not

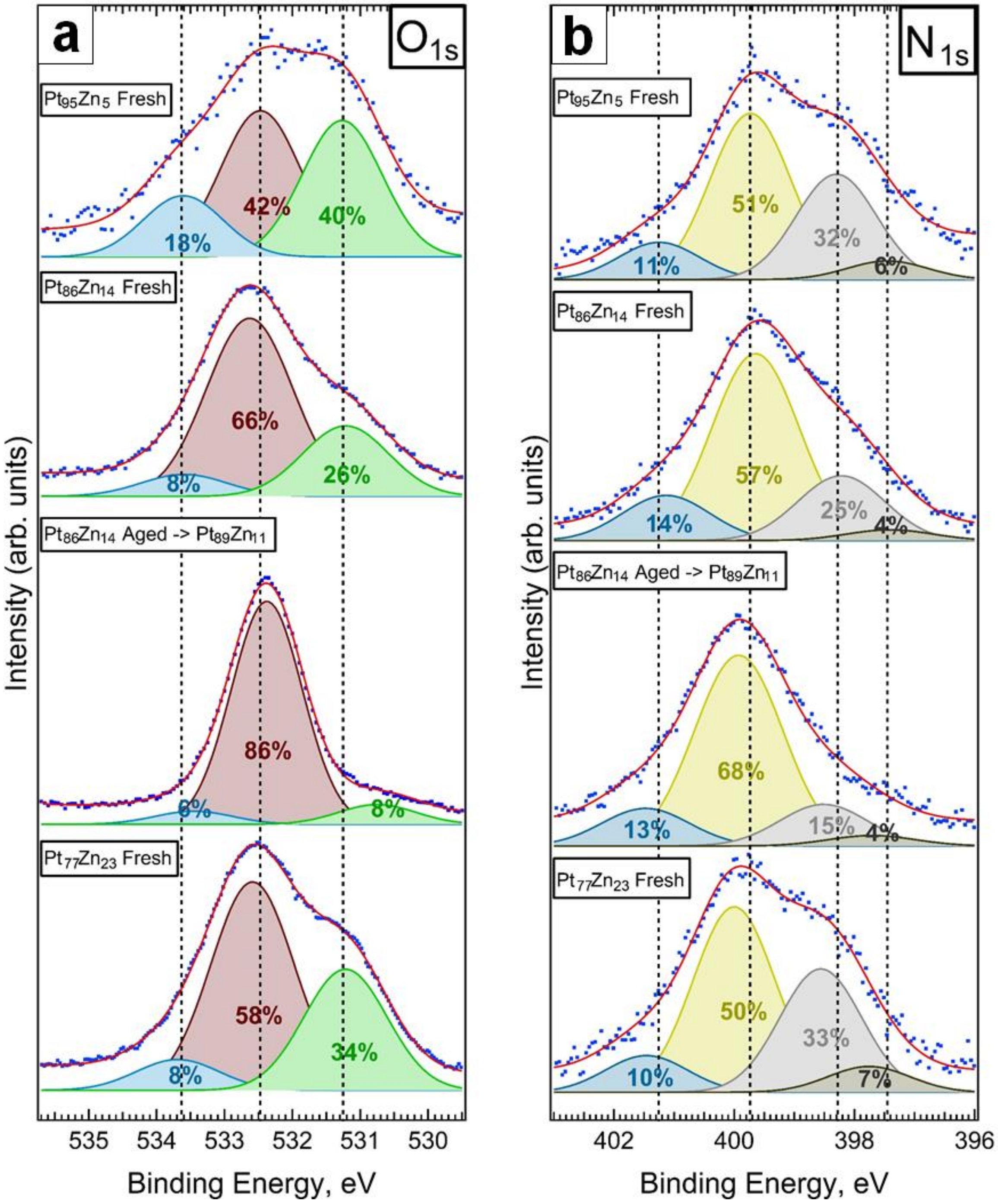

Figure 5. (a) O 1s and (b) N 1s spectra of the various Pt_xZn_y nanoparticles. The photon energy is 1486.7 eV (monochromatized Al K_α source). The overall energy resolution is better than 640 meV. Binding energy scales are uncorrected.

affected, and therefore no differential charging distorts the measurement. The decomposition of the N 1s of the pure ZnO particles dressed in oleylamine (discussed in SI, section S1) is different: only two components at 399.9 eV and 398.2 eV are necessary to fit the spectrum. Therefore, the components at 401 eV and 397.4 eV are specific to the presence of platinum. To interpret our XPS data, we will consider the mechanisms leading to the reduction of the metal cations in the two precursors, which necessarily implies the oxidation of the amine head.

Let us start with the intense component at 399.7 eV. This binding energy is that of an intact amine head ($R-CH_2-NH_2$). The amine can be in contact with a metallic surface, if dissociation is avoided, as in the case of 4-aminophenol deposited on Pt(111).[41] To the left of the main peak we see a component at 401 eV (~1.2 eV) from the main peak, specific to the presence of platinum. This high binding energy component can be ascribed to $R-CH_2-NH_2$ giving its lone pair to a Lewis acid site. For instance, dimethylamine bonds to Ti^{4+} sites on rutile with an N 1s binding energy of 401 eV.[42] Bonding to a Zn^{2+} ion (of the ZnO surface, or of the $Zn(acac)_2$ precursor) is excluded as it is absent in the N 1s spectrum of the ZnO nanoparticles. We take into consideration the fact that oleylamine ligands can substitute the two $acac^-$ anions around the Pt^{2+} cation, as it was shown in a MALDI–TOF mass spectroscopy study of the $Pt(acac)_2$ / oleylamine mixture.[43] Finally, we do not believe that the high binding energy component in the N 1s spectrum can be ascribed to a protonated head $R-CH_2-NH_3^+$, that is observed at 402 eV, as in zwitterionic aminoacids.[44]

Letting apart the non-dissociated amine head components, let us now consider the two lower binding components, at 398.4 eV and 397.4 eV that we will relate to decomposed amine heads. To identify the corresponding chemical functions, the best is to consider the reaction mechanisms leading to the reduction of metals in the presence of oleylamine. The [$-CH_2-NH_2$] unit is the provider of H atoms in the Pt(II) reaction mechanism, in which the platinum atom serves as a relay for the hydrogen atoms.[45,46,47,48] The following reactions are involved to produce the first Pt^0 atom:

$R\text{-}CH_2\text{-}NH_2 \rightarrow 2H + R\text{-}HC{=}NH$ (aldimine) (step 1)

$2H + Pt^{2+}(acac^-)_2 \rightarrow Pt^0 + 2\ Hacac$ (step 2)

Considering that the $(Pt)_n$ particle is formed, the nanocrystal surface serves now as a relay.[46] The amine decomposes (oxidizes) on a crystal facet to give an adsorbed aldimine and two adsorbed H (H_{ads}):

$R\text{-}CH_2\text{-}NH_{2\ ads} \rightarrow 2H_{ads} + R\text{-}HC{=}NH$ (step 1')

The aldimine molecule can further release two Hs to give a nitrile:

$R\text{-}HC{=}NH \rightarrow 2H_{ads} + R\text{-}C{\equiv}N$ (step 1'')

The adsorbed H can in turn reduce the metal cations in the incoming molecules $Pt(II)(acac)_2$ (through step 2) and $Zn(II)(acac)_2$ (through a step akin to step 2), thus enabling the growth of the alloy. Therefore, we expect the particle surface to be covered by $R\text{-}CH_2\text{-}NH_2$, and its decomposition products, that is, H_{ads} , $R\text{-}HC{=}NH$, and $R\text{-}C{\equiv}N$. Aldimine and nitrile species have been both clearly identified by infrared spectroscopy for the growth of silver nanoparticles in oleylamine.[46] Imines have a N 1s binding energy of 398.4 eV,[49] while nitriles adsorbed on Pt(111) and Ni(111) are found in the 397.2-397.7 eV range.[50] Therefore, considering the mechanisms involved in the growth of the particle, and the available XPS references, the N 1s component at 398.4 eV is attributed to an aldimine head ($R\text{-}HC{=}NH$) and that at 397.4 eV to a nitrile.[50] Note that the presence of an aldimine function, which is prone to hydrolization in the presence of moisture to give ammonia and a carbonyl compound, points to "clean" conditions during the growth process. The adsorption of the aldimine on the platinum surface may also have a stabilizing effect.

Adsorbate-controlled nanoparticle formation?

The shaping of the nanoparticles is usually explained in term of kinetic control (the production rate of the metal monomer in the solution) or in terms of adsorbate control.[22] Decreasing the reaction rate in the solution leads to equilibrium shapes, which would explain the transition from cuboids to cuboctahedra. However, we do not see how the ether could influence the rate in the solution.

Therefore, adsorbate control seems more relevant to the present case. Having in mind the chemical processes leading to the reduction of the precursor metallic cations, and the indication from N 1s XPS that oleylamine is partly dehydrogenated (oxidized), then we expect that H_{ads} and the ether additives are the species strongly bonded on the metal. The passivation of a particular surface by a bound ether can control nanoparticle formation by slowing the growth of one type of facet relative to the growth of other facets. Slowing down occurs because ether molecules and H_{ads} compete for the adsorption sites, and thus less H is available for reducing the incoming metallic cations. In our case, the binding strength of benzyl ether on the {100} facet would be greater than phenyl ether. Benzyl ether would block efficiently the growth of the {100} facets, which would lead to the preferred growth of cuboids. To explain why the spherical (cuboctahedral) particles grown in the presence of phenyl ether are richer in zinc, one must consider the binding strength of Zn atoms on the various facets. Zn should bind preferentially to Pt facets which possess more exposed surface atoms, since these surface atoms provide a high coordination number, and thus enhanced stability, for the deposited Zn atoms. The {100} facets are more open than the {111} ones, and therefore once the growth of the {100} is hindered, less zinc is incorporated.

Zinc Leaching in Toluene

When stored in toluene (not protected from air), and then washed in ethanol, 5 nm and 8 nm wide $Pt_{86}Zn_{14}$ particles tend to lose zinc. For both type of particles, the composition evolves to $Pt_{89}Zn_{11}$, as shown by EDX. These aged particles are denoted "$Pt_{86}Zn_{14} \rightarrow Pt_{89}Zn_{11}$" in the following.

HRTEM images of ~8 nm "$Pt_{86}Zn_{14} \rightarrow Pt_{89}Zn_{11}$" particles (stored 30 days in toluene) are shown in Figure 6. In images (a) and (b), the particles are in the (110) orientation (the beam axis is parallel to [110]). The (111) interplanar distances (0.22 ± 0.005 nm) of pure Pt are measured[25], but distortions are visible along the lattice planes crossing the particle centers. In image (c), the particle is in the (001) orientation (the beam axis is parallel to [001]). We observe (200) lattice plane of pure Pt (0.200.005 nm), except in the center where the resolution is lost. We find no hint of the Pt_3Zn characteristic plane (at 0.275 nm), in contrast to what was observed for the fresh particles. HRTEM suggests that a ~2 nm-thick well-organized pure Pt outer shell is formed around a core consisting in a disordered Pt-Zn alloy.

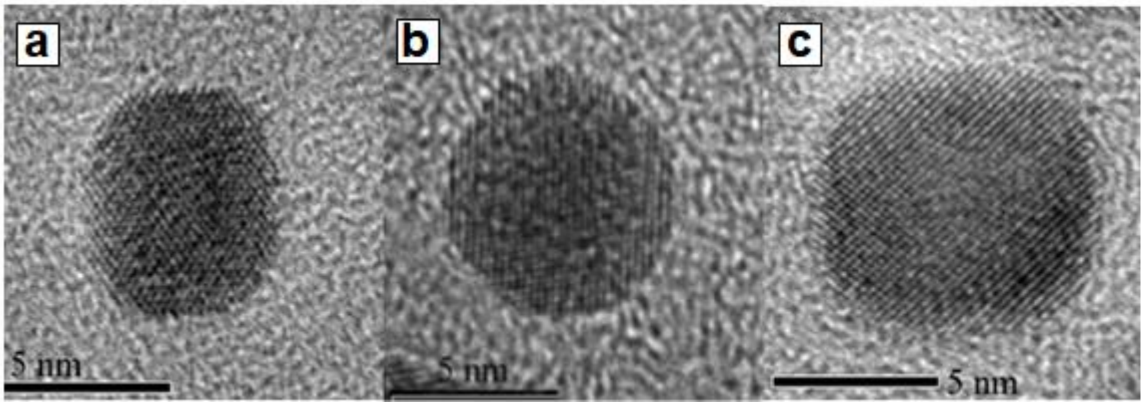

Figure 6. ~8 nm wide $Pt_{86}Zn_{14}$ nanoparticles stored one month in toluene where zinc-leaching is observed. The particle centers appear disordered. Bulk Pt planes are imaged at the periphery. In images (a) and (b), the particles are in the (110) orientation. In image (c), the particle is in the (001) orientation. The JEOL 3010 microscope is operated at 300 kV.

The core-level and Auger spectra of "$Pt_{86}Zn_{14} \rightarrow Pt_{89}Zn_{11}$" particle (5 nm wide) stored 4 days in toluene are shown in Figures 4 and 5. While the Pt 4f spectrum is not affected by ageing, zinc Auger and core-level spectra have changed dramatically. In the Auger spectrum (Figure 4, center), zinc atoms are now essentially in a metallic state (Zn^0), as the oxide component at a kinetic energy of 987 eV has practically vanished. The Zn $2p_{3/2}$ spectrum confirms this observation, as the 1022.8 eV component due to the oxide has also considerably diminished. It is very interesting to notice that the modified Auger parameter α' of Zn^0 equal to 2013.20 eV (Figure 4, center panel) is also indicative of Zn leaching, being now halfway between 2012.9 eV (Pt_3Zn) and 2013.4 eV (diluted Zn particles). The equivalent ZnO oxide thickness ($\eta_{ZnO} = 1$) estimated from equation [1] is 0.013 nm. As for the "fresh" Zn-poor $Pt_{95}Zn_5$ sample, the equivalent thickness is unrealistically thin, and thus large parts of the particle surface are uncovered by ZnO. Indeed, assuming a *h*-BN like monolayer (0.22 nm), $\eta_{ZnO} = 2\%$.

In the O 1s spectrum, the low binding energy component related to zinc oxide is now very weak. However, the component at ~533 eV remains. As most of the zinc oxide contribution is eliminated, this is a further evidence that this component is necessarily related to organic compounds. For its part, the N 1s spectrum shows that the particles are still dressed in oleylamine (note the intense component due to $R\text{-}CH_2\text{-}NH_2$ at 399.7 eV). We still observe components in the 398.2-397.2 eV range (attributed to aldimine and nitrile).

The toluene solution is not protected from air, therefore O_2 can be dissolved as traces. At 300 K the Henry coefficient is 105 MPa,[51] therefore the mole fraction of O_2 dissolved in toluene is $\sim 2\times10^{-4}$. We can expect that oxygen will oxidize preferentially the less noble metal, driving it out from the nanoparticle. Then oxidation in toluene should lead to the growth of ZnO scales around the particle. However, the aged samples examined so far ("$Pt_{86}Zn_{14} \rightarrow Pt_{89}Zn_{11}$") show exactly the opposite, as XPS indicates that their surface is practically free of zinc oxide, and TEM does not identify any zinc oxide phase. This conundrum can be answered if we consider that the oxide formed has been *separated* from the nanoparticle during washing in ethanol. The remaining metal particles then have a surface highly depleted in zinc (as shown in the TEM images) and are therefore resistant to oxidation during their passage in air before XPS analysis.

To ascertain the cause of zinc leaching, we have examined the zinc-richest particles $Pt_{77}Zn_{23}$, having in mind that, due to their high zinc content, the zinc oxide phase produced in toluene could be sufficiently abundant to be observed with the microscopic tools. Our hopes have been fulfilled. We show in Figure 7 the TEM image of fresh particles (Figure 7(a)), and that of particles stored one month in toluene and then washed in ethanol (Figure 7 (b)). The fresh particles, whose Zn $2p_{3/2}$ XPS spectra are given in Figure 4, have an equivalent oxide thickness of ~0.5 nm, but the TEM image 7(a) is not indicative of any ZnO phase. In contrast the TEM image 7(b) and HRTEM image 7(c) of the aged particles show that “sheets” decorated by darker Pt-containing metallic particles have made their appearance.

Unlike $Pt_{86}Zn_{14}$ particles, the zinc oxide grown from the $Pt_{77}Zn_{23}$ sample is not completely washed out after the ethanol treatments. This is proved by HRTEM. In image 7(d) we can image atomic rows and observe a hexagonal lattice with a parameter $a= 0.33 \pm 0.005$ nm, characteristic of wurtzite-ZnO (0.326 nm). In this case the electron beam is aligned with the c-axis of wurtzite. In another position, image 7(e), the beam is perpendicular to the c-axis. Then we observe sheets (~2-3 nm thick) made of parallel planes with a spacing of 0.26 nm (corresponding to the (002) planes of wurtzite).

A plausible scenario for the formation of the ZnO sheets is given in Figure 7 (f). Zinc is oxidized at the particle surface. Few layers of *h*-BN-like ZnO are formed until a critical thickness[39] is reached, above which the oxide is transformed into wurtzite ZnO. However, the particle is not passivated, oxidation goes on, producing thick oxide scales that cannot sustain the curvature of the particles and *detach*, leading to the sheets we observe here. At the end of the zinc leaching process, only ultrathin ZnO films remain on the metallic particle itself, whose surface is practically pure Pt.

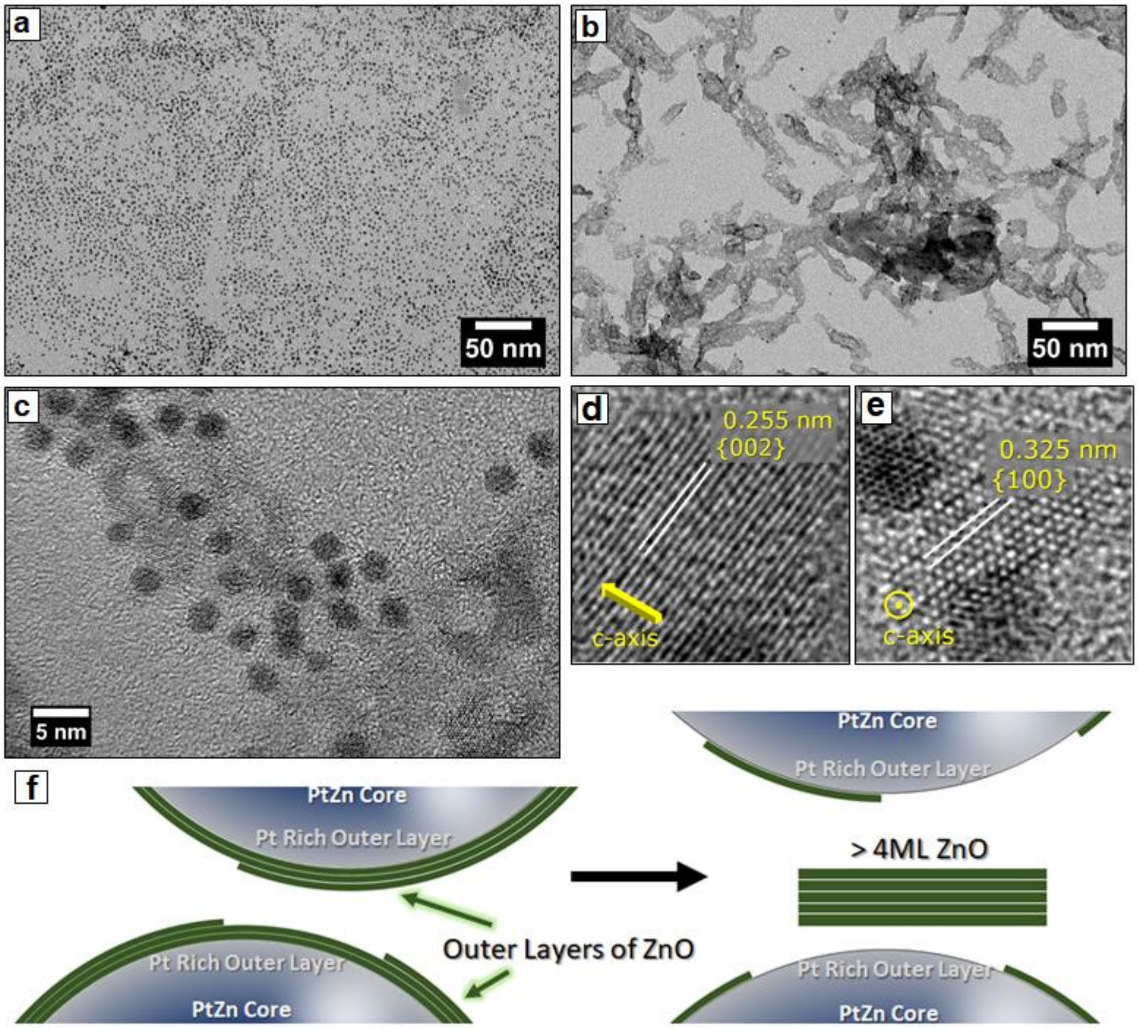

Figure 7. (a) TEM micrograph (JEOL1011 operated at 100 kV) of the "fresh" zinc-rich $Pt_{77}Zn_{23}$ particles; (b) the same particles after a one-month storage in toluene. (c) HRTEM image (JEOL JEM 2010 operated at 200 kV) of the sheet supporting the metallic particles that appear darker. Atomically resolved micrographs (d) Inset zoom in on the well-ordered structure of the ZnO veils (d) along the c-axis and (e) perpendicular to the c-axis. (f) A plausible mechanism explaining the formation of the ZnO sheets and the loss of zinc at the nanoparticle surface

TEM beam assisted Pt-Zn dealloying under O_2 pressure

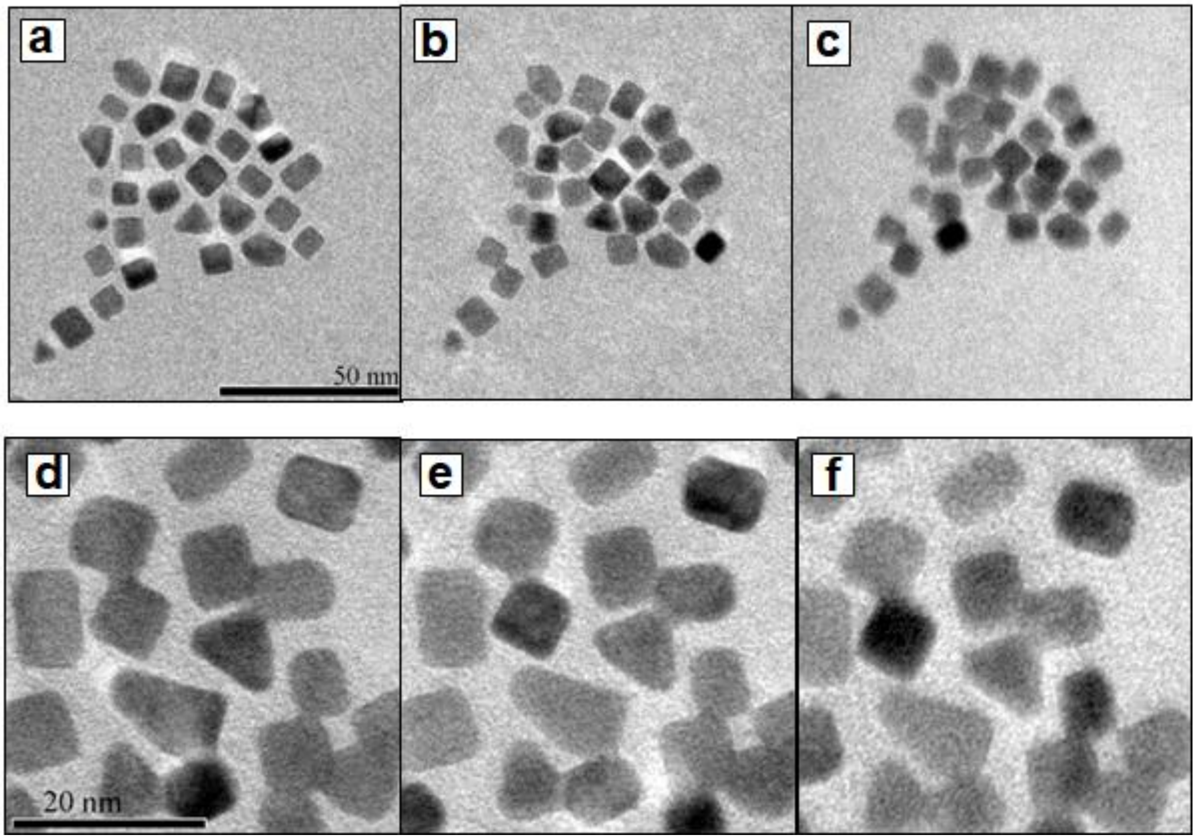

Figure 8. Environmental TEM images of “$Pt_{86}Zn_{14}\rightarrow Pt_{89}Zn_{11}$” particles exposed to O_2 (4 mbar) at room temperature in the environmental cell. For images (a-c), the magnification of the microscope, ×100,000, corresponds to a beam current density of 1.5 A/cm^2 on the sample: (a) vacuum, (b) 2 min in O_2, (c) 4 min in O_2. For images (d-f) the magnification of the microscope, ×300,000, corresponds to a beam current density of 13.5 A/cm^2 on the sample: (d) vacuum, (e) 2 min in O_2, (f) 4 min in O_2. The JEOL 3010 microscope is operated at 300 kV

“$Pt_{86}Zn_{14}\rightarrow Pt_{89}Zn_{11}$” particles (aged one month in toluene) were observed under a pressure of 4 mbar of pure O_2 in the sealed cell, at two magnifications, ×100,000 (beam current density of 1.5 $A.cm^{-2}$ on the sample) shown in Figure 8(a-c), and ×300,000 (beam current density of 13.5

A.cm^{-2} on the sample) shown in Figure 8(e-f). We recall that XPS indicates that these particles are terminated by ultrathin discontinuous ZnO layers.

Images 8 (a,d) are taken under vacuum. Images 8 (a,d) are taken under vacuum. The contrast and shape of the particle is always stable under strong irradiation conditions. This is expected as beam induced radiolytic damage in metals, unlike insulators, is expected to be weak.[52]

Images 8 (b,e) and 8 (c,f) are taken after exposures to O_2 of 2 and 4 min, respectively. Once O_2 is introduced, the particle corners tend to get rounded, due to the formation of facets of indexes higher than {100}, *i.e.* {111}, {112}, {113} *etc.*. The crucial point is that the contrast within particles evolves with time. All the observed phenomena (corner rounding and contrast changes with exposure time) are more pronounced for identical observation times when the current density is higher. This suggests that an increase of the beam current density by about an order of magnitude accelerates the phenomena. We attribute the spectacular contrast changes to a modification of the zinc content in the particles.

Since the observed transformations are due to the simultaneous presence of the beam and oxygen pressure, we must consider the processes that can lead to the activation of oxygen and to the *oxidation* of nanoparticles. Indeed, beam assisted oxidation of Pd metallic nanoparticles is reported during HRTEM measurements performed at 300 keV with a current density of 3.3 A cm^{-2} (intermediate between the conditions we used in this work) under an O_2 pressure of 2×10^{-6} mbar.[53] The phenomenon is not thermal and interpreted as due to O_2 decomposition into atomic oxygen that binds to the Pd surfaces, which leads eventually to the oxidation of facets of specific orientations. Oxidation likely occurs because adsorbed O_2 molecules are broken into atomic oxygen atoms by low energy secondary electrons[54] *via* an attachment-dissociation reaction.[55,56] Conversely, the beam can also provoke oxygen desorption from oxides due to a knock-on effect (sputtering)[52] or a Knotek-Feibelman effect.[57] The competition between the two opposite processes will be in favour of oxidation when the O_2 pressure will increase.[53]

Therefore, beam-assisted oxidation is also expected here, especially since the oxygen pressure is four orders of magnitude higher than in Ref.[53]. However, the situation is more complex than in the case of Pd oxidation, as we deal with bimetallic particles. Considering that the less noble metal will oxidize preferentially, as shown clearly by our XPS data, we can imagine that zinc oxide will grow at the periphery of the nanoparticle. As zinc is consumed at the surface, a zinc gradient is established between the core (richer in zinc) and the periphery (poorer in zinc), which explains the contrast changes.

CO adsorption affects the oleylamine bonding at the organic/inorganic interface

Low zinc content nanoparticles, $Pt_{95}Zn_5$ and $Pt_{89}Zn_{11}$ ($Pt_{86}Zn_{14}$ aged for 70 days in toluene) were exposed to the O_2:CO (4:1) mixture, under 1 mbar and at room temperature, in the preparation chamber of the XPS setup. Then the samples were examined by XPS in UHV without exposure to air. The Zn $2p_{3/2}$ spectra are shown in Figure 9, left panel. For $Pt_{95}Zn_5$, the Zn^{2+}:Zn^0 distribution of 19:81 corresponds to a continuous film ($\eta_{ZnO} = 1$) of equivalent ZnO thickness 0.014 nm, using equation [1]. Thus, the oxide film is discontinuous. The fraction η_{ZnO} of the surface covered by ZnO is 8%, assuming one monolayer of ZnO, and 4%, assuming a bilayer. The $Pt_{89}Zn_{11}$ sample is more oxidized. The Zn^{2+}:Zn^0 distribution of 46:54 for $Pt_{89}Zn_{11}$ leads to a

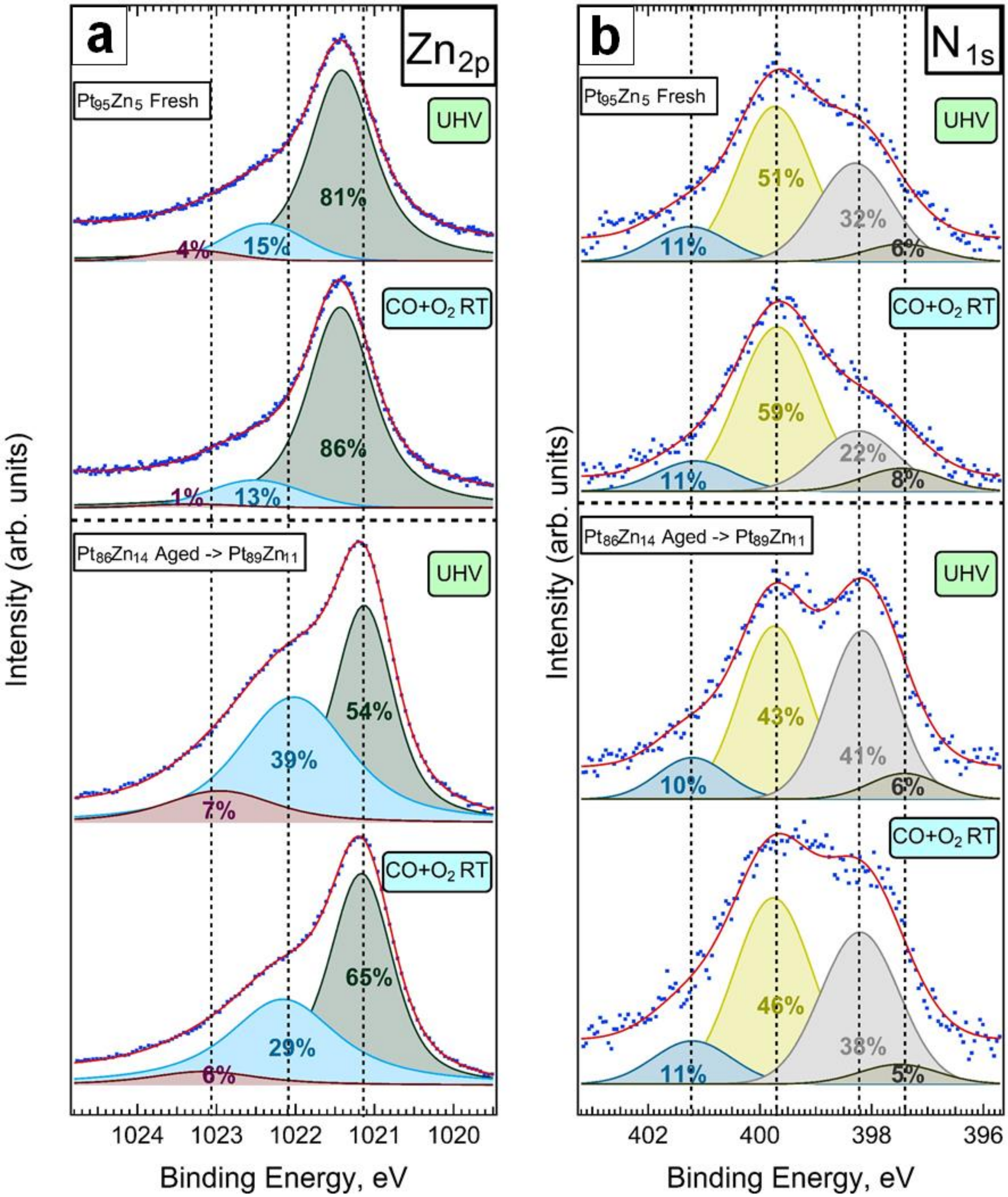
a
Zn2p
Pt95Zn5 Fresh
UHV
81%
15%
4%
CO+O2 RT
86%
13%
1%
Pt86Zn14 Aged -> Pt89Zn11
UHV
54%
39%
7%
CO+O2 RT
65%
29%
6%
1024
1023
1022
1021
1020
Binding Energy, eV
Intensity (arb. units)
b
N1s
Pt95Zn5 Fresh
UHV
51%
32%
11%
6%
CO+O2 RT
59%
22%
11%
8%
Pt86Zn14 Aged -> Pt89Zn11
UHV
43%
41%
10%
6%
CO+O2 RT
46%
38%
11%
5%
402
400
398
396
Binding Energy, eV
Intensity (arb. units)

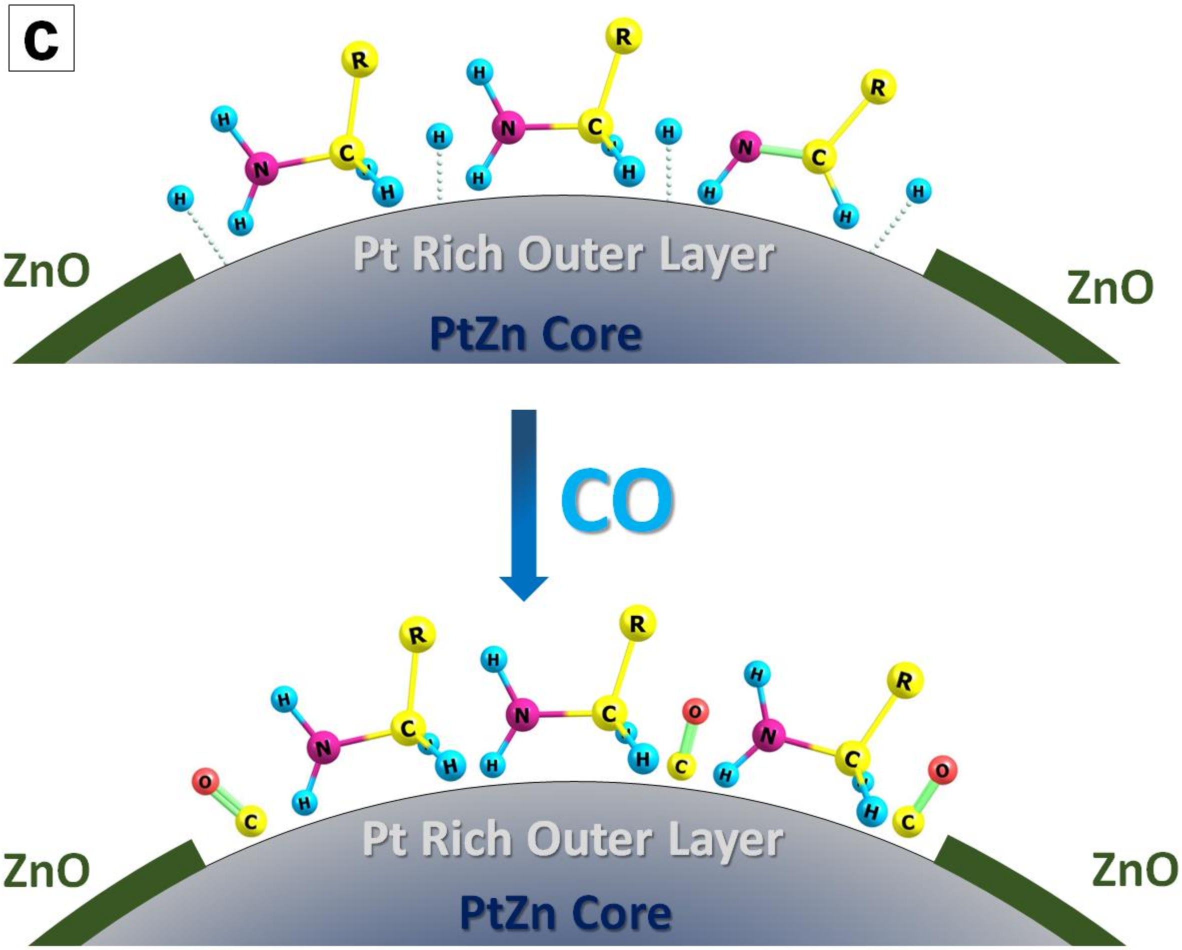

Figure 9. (a) Zn $2p_{3/2}$ and (b) N 1s XPS spectra of "70 days aged" $Pt_{86}Zn_{14} \rightarrow Pt_{89}Zn_{11}$ (average size ~5 nm) and of "fresh" $Pt_{95}Zn_{5}$ (average size ~ 11 nm). The measurements were made in UHV before and after exposure to the O_2:CO mixture (4:1, 1 mbar total pressure) at room temperature. (c) Plausible explanation to changes due to CO exposure: H displacement by CO and aldimine reduction into amine.

continuous film ($\eta_{ZnO} = 1$) of equivalent thickness 0.11 nm. Considering again that the ZnO film is discontinuous, we find that η_{ZnO}=58% for one monolayer of ZnO, and 31% for a bilayer. Consequently, for both particles large fraction of their surface area is terminated by Pt.

After exposure to the gas mixture, the Zn^{2+} component in the $2p_{3/2}$ spectra tends to decrease with respect to the Zn^0 one, for both samples. This can be interpreted as due to a reduction in size of the ZnO patches present on the platinum surface (see equation [1]). Indeed for a ZnO monolayer on Pt(111) exposed to the O_2:CO mixture at room temperature (same composition and pressure as in the present case), STM shows that CO adsorption de-wets the ZnO films, whose patches tend to shrink as bilayers form.[9] Considering the adsorption energies on clean ZnO (0.17-0.28 eV)[58] and clean Pt surfaces (1.3-1.45 eV),[59,60] CO prefers clearly Pt to ZnO. By bonding exclusively to platinum areas, CO can displace the zinc oxide layer.

The N 1s spectra, shown in the right panel of Figure 9, carry the most interesting information. A clear change is seen in the aldimine component (R-CH=NH) at 398.3 eV which is depressed after gas exposure. Therefore, *CO induces a chemical reaction that tends to eliminate the aldimine species at room temperature.* Our interpretation is the following. We must not forget that H atoms are likely adsorbed on Pt areas, due to the successive oxidations of the amine head to aldimine and nitrile. Then surface science studies indicate that CO is able to dislodge H atoms adsorbed on Pt(111).[61] The effect of CO adsorption at room temperature on the aldimine component suggests that H atoms desorbing from the surface react with the aldimine that could be reduced (see Figure 9(c)).

CONCLUSIONS

Pt-Zn nanoparticles with a wide range of composition ($Pt_{77}Zn_{23}$, $Pt_{86}Zn_{14}$ and $Pt_{95}Zn_5$), shape (from spherical to cuboidal) and size were produced at 350°C in oleylamine from $Pt(acac)_2$ and $Zn(acac)_2$ precursors and their shape, structure and interface chemistry was studied by a combination of electron microscopy and X-ray photoelectron and Auger spectroscopies. Structural and chemical information converge to show that the particles formed are alloys and not assemblies of pure platinum and zinc oxide. By cross-referencing the average composition and spectroscopic data, we found a correlation between the zinc concentration and the value of the modified auger parameter of metallic zinc that appears as a good proxy for monitoring zinc leaching phenomena.

We show that the ether additive has a strong impact both on the morphology and composition. Phenyl ether favors spherical particles with a zinc content close to that of the ordered intermetallic Pt_3Zn. Unlike phenyl ether, benzyl ether favors cuboidal Pt-Zn particles with a lower zinc content (≤14%). In those particles the zinc distribution is certainly inhomogeneous, as the Pt_3Zn intermetallic phase is detected by electron microscopy. XPS spectra shows that after a short exposure to air, the particle surface is oxidized. While we have no indication of platinum oxidation from XPS, zinc is oxidized. Discontinuous ultrathin films are formed on $Pt_{95}Zn_5$. For higher zinc content particles, $Pt_{86}Zn_{14}$ and $Pt_{77}Zn_{23}$, a ZnO film with an equivalent thickness of about two monolayers grows on the particle surface (there are spectroscopic hints that it is also discontinuous and locally thicker). The chemistry at the interface between the metallic particle and the oleylamine ligand shell is now better understood thanks to the XPS investigation. The N 1s spectra show several components attributable to the reactants and products of the metal cation reduction processes. We observed the signature of the intact amine reactant/ligand (the dominant species) and of its de-hydrogenation (oxidation) products, aldimine and nitrile. Amine heads making a dative bond with a Lewis site are also identified, likely a Pt^{2+} ion in an oleylamine-acac-Pt^{2+} complex.

All analytical tools (electron microscopy and photoelectron spectroscopy) concur in showing that the particles are not chemically stable under prolonged oxidation in non-degassed toluene. Zn-leaching is observed in all cases. Pt_3Zn gives way to a disordered alloy surrounded by a pure Pt shell. The driving force is the oxidation of the less noble metal, more oxophilic metal of the alloy, because of oxygenated species dissolved in the solution. This is clearly demonstrated by the zinc-richest particles spherical $Pt_{77}Zn_{23}$, for which microscopy shows that Zn leaving the particle forms extended wurtzite ZnO sheets on which the Zn depleted particles are attached, even after washing in ethanol. Unlike Zn-rich $Pt_{77}Zn_{23}$, the aged cuboidal particles $Pt_{86}Zn_{14}$, do not exhibit wurtzite “veils”, their surface being partially covered by patches of ultrathin ZnO layers. This suggests that the detached ZnO scales are lost by washing. Particle dealloying under a 300 keV TEM beam is also observed, only when a partial pressure of O_2 (4 mbar) is introduced. This is further evidence that oxidation drives compositional changes in nanoparticles.

XPS gives us also an evidence, albeit indirect, that H atoms resulting from the oxidation of the amine heads are adsorbed on Pt. As a matter of fact, the N 1s aldimine component is labile, being depressed by an exposure to CO at room temperature. We propose that this change is due to H atom removal from the platinum particle surface by preferential CO adsorption and further reaction with the aldimine.

The observations we made on the chemical evolution of these Pt-Zn nanoparticles are also relevant to electrocatalysis. The surface chemistry observed for the low zinc fresh $Pt_{95}Zn_5$ particles and the aged $Pt_{89}Zn_{11}$ ones appears ideal to oxidize CO adsorbed on Pt which is an intermediate in the oxidation of CH_3OH (MOR). Ultrathin ZnO films patches on platinum surfaces eventually corresponds to the definition of an inverse oxide/metal catalyst (according to Hrbek and Rodríguez). It is likely that H released during the reduction of the metal cations by the amine will also form hydroxyl species on the ZnO patches. This may explain the more facile oxidation process of CO to CO_2 *via* a carboxyl intermediate at the boundary of the ZnO and Pt areas (that was identified on the ZnO/Pt(111) model catalyst[9]), and thus the success of Pt-Zn nanoparticles in MOR.[13,17]

EXPERIMENTAL DETAILS

Synthesis

We basically followed the method indicated by Kang *et al.*,[17] while reducing the solution volumes used by a factor of 4. $Pt(acac)_2$ and $Zn(acac)_2$ precursors were dissolved in a solution of oleylamine (3.9 ml) under N_2 atmosphere. The solution was brought to 350 °C, as recommended by Kang *et al.* and kept at this high temperature for 5 min. Then the reaction mixture was cooled down and purified in ethanol. After centrifugation, the nanoparticle precipitate was dispersed in toluene.

With a $Pt(acac)_2$: $Zn(acac)_2$ ratio of 1:1 molar ratios (0.02 g of $Pt(acac)_2$ and 0.0125 g of $Zn(acac)_2$) and in the presence of *benzylether* (2,5 ml), we produced cuboidal $Pt_{86}Zn_{14}$ nanoparticles, the average composition were checked by Energy-dispersive X-ray spectroscopy EDX). Bubbling argon into oleylamine prior to synthesis diminishes the concentration of moisture and oxygen in the solvent. This has an effect on the particle size that reached ~8 nm, instead of ~5 nm without bubbling.

With the same $Pt(acac)_2$: $Zn(acac)_2$ ratio of 1:1, but in the presence of phenyl ether (2.0 ml), we produced smaller (~2.8 nm) *spherical* particles that had a composition $Pt_{77}Zn_{23}$, closer to that of the intermetallic ordered compound Pt_3Zn ($AuCu_3$ –type).[17] The influence of the ether additive on particle morphology is in line with the findings of Kang *et al.*.[17] We were also able to produce zinc-poor $Pt_{95}Zn_5$ cuboidal particles using a high $Pt(acac)_2$: $Zn(acac)_2$ ratio of 10:1 (0.0354 g of $Pt(acac)_2$ and 0.0026 g of $Zn(acac)_2$). The synthesis of such particles was not reported yet.

The summary of the syntheses is given in Table 1.

Table 1. Summary of the synthesis products ("fresh") obtained in oleylamine at 350°C, according to the $Pt(acac)_2$: $Zn(acac)_2$ ratio and the ether additive. (*) purified oleylamine by argon bubbling.

$Pt(acac)_2$:$Zn(acac)_2$	Additive	Composition (EDX)	Average size(nm)/shape
10:1	benzylether	$Pt_{95}Zn_5$	9.4 nm/cuboidal
1:1	benzylether	$Pt_{86}Zn_{14}$	5 or 8* nm/cuboidal
1:1	phenylether	$Pt_{77}Zn_{23}$	2.8 nm/spherical

The synthesis procedure is not optimized for pure Pt, since working at 350°C with $Pt(acac)_2$ alone in oleylamine leads to non-uniform agglomerated nanoparticles, likely because the growth temperature was probably too high. The growth temperature is therefore only suitable to produce bimetallic Pt-Zn particles. Conversely, using $Zn(acac)_2$ alone in oleylamine, we obtained only wurtzite ZnO nanoparticles, in agreement with previous findings.[17,62] The full formation mechanism ZnO nanocrystals by the decomposition of metal acetylacetonate in oleylamine is not clear. Metallic zinc is probably immediately oxidized by traces of oxygen or moisture.[62] Detailed electron microscopy and XPS investigations of pure ZnO particles are given in the Supporting Information (SI), section S1.

Sample Characterization

Scanning Electron Microscopy. To determine the average composition of the PtZn nanocrystals with a good accuracy, the EDX analyzer of an SEM JEOL 5510LV microscope is used, following a protocol already established for nanoalloys.[63] A film of nanocrystals is made by slow evaporation at room temperature of a concentrated solution of nanocrystals in toluene. The resulting film (Figure S3 in the SI) was thicker than 10 µm and presented the characteristic flaky appearance due to the drying process. We show also in Figure S3 a typical energy-dispersive X-ray spectrum (EDX) of PtZn nanoparticles.

Transmission Electron Microscopy Measurements. Transmission electron microscopy (TEM) images are obtained using a JEOL1011 operated at 100 kV with magnifications up to 500000×. Images are obtained with a Gatan digital camera. TEM samples are prepared by the drop deposition method on an amorphous carbon coated TEM grid. High Resolution TEM imaging was carried out with a JEOL JEM 2010 equipped with a Gatan digital camera operated at 200 kV.

Environmental TEM. The Pt-Zn nanoparticles were observed *in situ* and in real time under near-ambient gas pressure (4 mbar) in a sample holder sealed with a thin carbon membrane.[64] We used a standard JEOL 3010 microscope operated at 300 kV. Additional HRTEM images were also obtained with the same microscope.

X-Ray Photoelectron Spectroscopy. Samples for XPS measurements were prepared by drop deposition of concentrated nanoparticle solutions in toluene on a gold-on-mica substrate. After allowing the solvent to evaporate, the samples were induced in the XPS setup *via* a fast entry loadlock. The XPS experiments are carried out with a PHOIBOS 150 spectrometer from SPECS, fitted with a delay line detector. We use an Al K_α monochromatized source (1486.7 eV).

The total resolution (source and spectrometer) is 640 meV. The inelastic mean free paths (IMFP) of the core-level and Auger electrons depend on their kinetic energies. The calculated[65] inelastic mean free paths (IMFPs) can be found in Table 2. They can be usefully compared to the known particle sizes (Table 1) and the oleylamine ligand thickness (Figure 1).

Table 2. Calculated[65] inelastic mean free paths in bulk platinum, bulk ZnO, and oleylamine.

Kinetic Energy (Peak)	λ, nm in ZnO	λ, nm in Pt	λ, nm in oleylamine
465 eV (Zn 2p)	1.132	0.780	1.564
994 eV (Zn $L_3M_{4,5}M_{4,5}$)	1.963	1.301	2.815
1087 (N 1s)	-	-	3.022
1415 eV (Pt 4f)	2.574	1.534	3.742

SUPPORTING INFORMATION

The Supporting Information is available free of charge *via* the Internet at http://pubs.acs.org.

Figure S1: TEM micrographs of ZnO nanoparticles.

Figure S2: Zn $2p_{3/2}$, $L_3M_{4,5}M_{4,5}$ Zn Auger, O 1s and N 1s spectra of pure ZnO nanocrystals.

Figure S3: Energy-dispersive X-ray analysis spectrum of PtZn nanoparticles.

Figure S4: SAED patterns of pure Pt and "fresh $Pt_{86}Zn_{14}$" particles.

Figure S5: $Zn2p_{3/2}$ spectrum of $Pt_{86}Zn_{14}$ NPs aged for 1 year.

ACKNOWLEDGEMENTS

This work was supported by the LabEx MiChem, part of French State Funds managed by the Agence Nationale de la Recherche (ANR) within the "*Investissements d'Avenir*" program under reference ANR-11-IDEX-0004-02. Alter Zakhtser gratefully acknowledge the funding received towards his PhD from LabEX MiCHEM. The recent upgrade of the XPS platform (Institut Parisien de Chimie Physique et Théorique) received support from the ANR, *via* the project entitled "Nucleation, growth and reactivity of MEtallic and bimetallic Nanocrystals" (NUMEN) under reference ANR-17-CE09-0037. The authors would also like to thank the staff of the electron microscopy platform of the "Laboratoire de Réactivité de Surface" (LRS), Sorbonne Université.

CORRESPONDING AUTHORS

Ahmed Naitabdi E-mail : ahmed.nait_abdi@sorbonne-universite.fr;

François Rochet E-mail : francois.rochet@sorbonne-universite.fr;

Caroline Salzemann E-mail : caroline.salzemann@sorbonne-universite.fr;

REFERENCES

(1) Sattler, J. J. H. B.; Ruiz-Martinez, J.; Santillan-Jimenez, E.; Weckhuysen, B. M. Catalytic Dehydrogenation of Light Alkanes on Metals and Metal Oxides. *Chem. Rev.* **2014**, *114*, 10613–10653.

(2) Campbell, C. T.; Ertl, G.; Kuipers, H.; Segner, J. A Molecular Beam Study of the Catalytic Oxidation of CO on a Pt(111) Surface. *J. Chem. Phys.* **1980**, *73*, 5862–5873.

(3) Gao, F.; Wang, Y.; Cai, Y.; Goodman, D. W. CO Oxidation on Pt-Group Metals from Ultrahigh Vacuum to Near Atmospheric Pressures. 2. Palladium and Platinum. *J. Phys. Chem. C* **2009**, *113*, 174–181.

(4) Gao, F.; Wang, Y.; Goodman, D. W. Reply to "Comment on 'CO Oxidation on Pt-Group Metals from Ultrahigh Vacuum to Near Atmospheric Pressures. 2. Palladium and Platinum.'" *J. Phys. Chem. C* **2010**, *114*, 6874.

(5) Liu, G.; Zeng, L.; Zhao, Z. J.; Tian, H.; Wu, T.; Gong, J. Platinum-Modified ZnO/Al2O3 for Propane Dehydrogenation: Minimized Platinum Usage and Improved Catalytic Stability. *ACS Catal.* **2016**, *6*, 2158–2162.

(6) Rodríguez, J. A.; Hrbek, J. Inverse Oxide/Metal Catalysts: A Versatile Approach for Activity Tests and Mechanistic Studies. *Surf. Sci.* **2010**, *604*, 241–244.

(7) Burnett, D. J.; Capitano, A. T.; Gabelnick, A. M.; Marsh, A. L.; Fischer, D. A.; Gland, J. L. In-Situ Soft X-Ray Studies of CO Oxidation on the Pt(111) Surface. *Surf. Sci.* **2004**, *564*, 29–37.

(8) Sun, D.; Gu, X.-K.; Ouyang, R.; Su, H.-Y.; Fu, Q.; Bao, X.; Li, W.-X. Theoretical Study

of the Role of a Metal–Cation Ensemble at the Oxide–Metal Boundary on CO Oxidation. *J. Phys. Chem. C* **2012**, *116*, 7491–7498.

(9) Liu, H.; Zakhtser, A.; Naitabdi, A.; Rochet, F.; Bournel, F.; Salzemann, C.; Petit, C.; Gallet, J.-J.; Jie, W. Operando Near-Ambient Pressure X-Ray Photoelectron Spectroscopy Study of the CO Oxidation Reaction on the Oxide/Metal Model Catalyst ZnO/Pt(111). *ACS Catal.* **2019**, *9*, 10212–10225.

(10) Fu, Q.; Li, W.-X.; Yao, Y.; Liu, H.; Su, H.-Y.; Ma, D.; Gu, X.-K.; Chen, L.; Wang, Z.; Zhang, H.; Wang, B.; Bao, X. Interface-Confined Ferrous Centers for Catalytic Oxidation. *Science (80-.).* **2010**, *328*, 1141–1144.

(11) Mu, R.; Fu, Q.; Xu, H.; Zhang, H.; Huang, Y.; Jiang, Z.; Zhang, S.; Tan, D.; Bao, X. Synergetic Effect of Surface and Subsurface Ni Species at Pt−Ni Bimetallic Catalysts for CO Oxidation. *J. Am. Chem. Soc.* **2011**, *133*, 1978–1986.

(12) Martynova, Y.; Liu, B.-H.; McBriarty, M. E.; Groot, I. M. N.; Bedzyk, M. J.; Shaikhutdinov, S.; Freund, H.-J. CO Oxidation over ZnO Films on Pt(111) at near-Atmospheric Pressures. *J. Catal.* **2013**, *301*, 227–232.

(13) Rößner, L.; Armbrüster, M. Electrochemical Energy Conversion on Intermetallic Compounds: A Review. *ACS Catal.* **2019**, *9*, 2018–2062.

(14) Stamenkovic, V. R.; Mun, B. S.; Arenz, M.; Mayrhofer, K. J. J.; Lucas, C. A.; Wang, G.; Ross, P. N.; Markovic, N. M. Trends in Electrocatalysis on Extended and Nanoscale Pt-Bimetallic Alloy Surfaces. *Nat. Mater.* **2007**, *6*, 241–247.

(15) Stamenković, V.; Schmidt, T. J.; Ross, P. N.; Marković, N. M. Surface Segregation Effects

in Electrocatalysis: Kinetics of Oxygen Reduction Reaction on Polycrystalline Pt 3 Ni Alloy Surfaces. *J. Electroanal. Chem.* **2003**, *554–555*, 191–199.

(16) Sode, A.; Li, W.; Yang, Y.; Wong, P. C.; Gyenge, E.; Mitchell, K. A. R.; Bizzotto, D. Electrochemical Formation of a Pt/Zn Alloy and Its Use as a Catalyst for Oxygen Reduction Reaction in Fuel Cells. *J. Phys. Chem. B* **2006**, *110*, 8715–8722.

(17) Kang, Y.; Pyo, J. B.; Ye, X.; Gordon, T. R.; Murray, C. B. Synthesis, Shape Control, and Methanol Electro-Oxidation Properties of Pt-Zn Alloy and Pt 3Zn Intermetallic Nanocrystals. *ACS Nano* **2012**, *6*, 5642–5647.

(18) Chen, Q.; Zhang, J.; Jia, Y.; Jiang, Z.; Xie, Z.; Zheng, L. Wet Chemical Synthesis of Intermetallic Pt 3 Zn Nanocrystals via Weak Reduction Reaction Together with UPD Process and Their Excellent Electrocatalytic Performances. *Nanoscale* **2014**, *6*, 7019–7024.

(19) Wu, W.; Shevchenko, E. V. The Surface Science of Nanoparticles for Catalysis: Electronic and Steric Effects of Organic Ligands. *J. Nanoparticle Res.* **2018**, *20*, 255.

(20) Kwon, S. G.; Krylova, G.; Sumer, A.; Schwartz, M. M.; Bunel, E. E.; Marshall, C. L.; Chattopadhyay, S.; Lee, B.; Jellinek, J.; Shevchenko, E. V. Capping Ligands as Selectivity Switchers in Hydrogenation Reactions. *Nano Lett.* **2012**, *12*, 5382–5388.

(21) Sánchez-Sánchez, C. M.; Solla-Gullón, J.; Vidal-Iglesias, F. J.; Aldaz, A.; Montiel, V.; Herrero, E. Imaging Structure Sensitive Catalysis on Different Shape-Controlled Platinum Nanoparticles. *J. Am. Chem. Soc.* **2010**, *132*, 5622–5624.

(22) Personick, M. L.; Mirkin, C. A. Making Sense of the Mayhem behind Shape Control in

the Synthesis of Gold Nanoparticles. *J. Am. Chem. Soc.* **2013**, *135*, 18238–18247.

(23) Wang, Z. L. Transmission Electron Microscopy of Shape-Controlled Nanocrystals and Their Assemblies. *J. Phys. Chem. B* **2002**, *104*, 1153–1175.

(24) Taleb, A.; Petit, C.; Pileni, M. P. Synthesis of Highly Monodisperse Silver Nanoparticles from AOT Reverse Micelles: A Way to 2D and 3D Self-Organization. *Chem. Mater.* **1997**, *9*, 950–959.

(25) Long, N. V.; Chien, N. D.; Hayakawa, T.; Hirata, H.; Lakshminarayana, G.; Nogami, M. The Synthesis and Characterization of Platinum Nanoparticles: A Method of Controlling the Size and Morphology. *Nanotechnology* **2010**, *21*.

(26) Hynes, A. P.; Doremus, R. H.; Siegel, R. W. Sintering and Characterization of Nanophase Zinc Oxide. *J. Am. Ceram. Soc.* **2002**, *85*, 1979–1987.

(27) Egelhoff, W. F. Core-Level Binding-Energy Shifts at Surfaces and in Solids. *Surf. Sci. Rep.* **1987**, *6*, 253–415.

(28) Rodriguez, J. A.; Kuhn, M. Chemical and Electronic Properties of Pt in Bimetallic Surfaces: Photoemission and CO-chemisorption Studies for Zn/Pt(111). *J. Chem. Phys.* **1995**, *102*, 4279–4289.

(29) Zuo, J.; Erbe, A. Optical and Electronic Properties of Native Zinc Oxide Films on Polycrystalline Zn. *Phys. Chem. Chem. Phys.* **2010**, *12*, 11467–11476.

(30) Ballerini, G.; Ogle, K.; Barthés-Labrousse, M. G. The Acid-Base Properties of the Surface of Native Zinc Oxide Layers: An XPS Study of Adsorption of 1,2-Diaminoethane. *Appl. Surf. Sci.* **2007**, *253*, 6860–6867.

(31) Yi, L.; Wei, W.; Zhao, C.; Yang, C.; Tian, L.; Liu, J.; Wang, X. Electrochemical Oxidation of Sodium Borohydride on Carbon Supported Pt-Zn Nanoparticle Bimetallic Catalyst and Its Implications to Direct Borohydride-Hydrogen Peroxide Fuel Cell. *Electrochim. Acta* **2015**, *158*, 209–218.

(32) Moretti, G. Auger Parameter and Wagner Plot in the Characterization of Chemical States by X-Ray Photoelectron Spectroscopy: A Review. *J. Electron Spectros. Relat. Phenomena* **1998**, *95*, 95–144.

(33) Moretti, G. The Wagner Plot and the Auger Parameter as Tools to Separate Initial- and Final-State Contributions in X-Ray Photoemission Spectroscopy. *Surf. Sci.* **2013**, *618*, 3–11.

(34) Rössler, N.; Kotsis, K.; Staemmler, V. Ab Initio Calculations for the Zn 2s and 2p Core Level Binding Energies in Zn Oxo Compounds and ZnO. *Phys. Chem. Chem. Phys.* **2006**, *8*, 697–706.

(35) Fidelis, I.; Stiehler, C.; Duarte, M.; Enderlein, C.; Silva, W. S.; Soares, E. A.; Shaikhutdinov, S.; Freund, H. J.; Stavale, F. Electronic Properties of Ultrathin O-Terminated ZnO (0001¯)on Au (111). *Surf. Sci.* **2019**, *679*, 259–263.

(36) Koitaya, T.; Yamamoto, S.; Shiozawa, Y.; Yoshikura, Y.; Hasegawa, M.; Tang, J.; Takeuchi, K.; Mukai, K.; Yoshimoto, S.; Matsuda, I.; Yoshinobu, J. CO 2 Activation and Reaction on Zn-Deposited Cu Surfaces Studied by Ambient-Pressure X-Ray Photoelectron Spectroscopy. *ACS Catal.* **2019**, *9*, 4539–4550.

(37) Janotti, A.; Van de Walle, C. G. Fundamentals of Zinc Oxide as a Semiconductor. *Reports*

Prog. Phys. **2009**, *72*, 126501.

(38) Heinhold, R.; Williams, G. T.; Cooil, S. P.; Evans, D. A.; Allen, M. W. Influence of Polarity and Hydroxyl Termination on the Band Bending at ZnO Surfaces. *Phys. Rev. B - Condens. Matter Mater. Phys.* **2013**, *88*, 38–40.

(39) Tusche, C.; Meyerheim, H. L.; Kirschner, J. Observation of Depolarized ZnO(0001) Monolayers: Formation of Unreconstructed Planar Sheets. *Phys. Rev. Lett.* **2007**, *99*, 026102.

(40) Briggs, D.; Beamson, G. XPS Studies of the Oxygen 1s and 2s Levels in a Wide Range of Functional Polymers. *Anal. Chem.* **1993**, *65*, 1517–1523.

(41) Otero-Irurueta, G.; Martínez, J. I.; Bueno, R. A.; Palomares, F. J.; Salavagione, H. J.; Singh, M. K.; Méndez, J.; Ellis, G. J.; López, M. F.; Martín-Gago, J. A. Adsorption and Coupling of 4-Aminophenol on Pt(111) Surfaces. *Surf. Sci.* **2016**.

(42) Farfan-Arribas, E.; Madix, R. J. Characterization of the Acid−Base Properties of the TiO 2 (110) Surface by Adsorption of Amines. *J. Phys. Chem. B* **2003**, *107*, 3225–3233.

(43) Yin, X.; Shi, M.; Wu, J.; Pan, Y.-T.; Gray, D. L.; Bertke, J. A.; Yang, H. Quantitative Analysis of Different Formation Modes of Platinum Nanocrystals Controlled by Ligand Chemistry. *Nano Lett.* **2017**, *17*, 6146–6150.

(44) Reichert, J.; Schiffrin, A.; Auwä, W.; Weber-Bargioni, A.; Marschall, M.; Dell'angela, M.; Cvetko, D.; Bavdek, G.; Cossaro, A.; Morgante, A.; Barth, J. V. L-Tyrosine on Ag(111): Universality of the Amino Acid 2D Zwitterionic Bonding Scheme? **2010**.

(45) Man, R. W. Y.; Brown, A. R. C.; Wolf, M. O. Mechanism of Formation of Palladium

Nanoparticles: Lewis Base Assisted, Low-Temperature Preparation of Monodisperse Nanoparticles. *Angew. Chemie Int. Ed.* **2012**, *51*, 11350–11353.

(46) Chen, M.; Feng, Y.-G.; Wang, X.; Li, T.-C.; Zhang, J.-Y.; Qian, D.-J. Silver Nanoparticles Capped by Oleylamine: Formation, Growth, and Self-Organization. *Langmuir* **2007**, *23*, 5296–5304.

(47) Hiramatsu, H.; Osterloh, F. E. A Simple Large-Scale Synthesis of Nearly Monodisperse Gold and Silver Nanoparticles with Adjustable Sizes and with Exchangeable Surfactants. *Chem. Mater.* **2004**, *16*, 2509–2511.

(48) Capdevielle, P.; Lavigne, A.; Sparfel, D.; Baranne-Lafont, J.; Nguyen, K. C.; Maumy, M. Mechanism of Primary Aliphatic Amines Oxidation to Nitriles by the Cuprous Chloride - Dioxygen - Pyridine System. *Tetrahedron Lett.* **1990**, *31*, 3305–3308.

(49) Dziembaj, R.; Piwowarska, Z. X-Ray Photoelectron Spectroscopy (XPS) as a Useful Tool to Characterize Polyaniline Doped by 12-Tungstosilicic, 12-Tungstophosphoric and 12-Molybdophosphoric Acids. *Synth. Met.* **1994**, *63*, 225–232.

(50) Chen, J. J.; Winograd, N. The Adsorption and Decomposition of Methylamine on Pd{111}. *Surf. Sci.* **1995**, *326*, 285–300.

(51) Li, A.; Tang, S.; Tan, P.; Liu, C.; Liang, B. Measurement and Prediction of Oxygen Solubility in Toluene at Temperatures from 298.45 K to 393.15 K and Pressures up to 1.0 MPa. *J. Chem. Eng. Data* **2007**, *52*, 2339–2344.

(52) Egerton, R. F. Control of Radiation Damage in the TEM. *Ultramicroscopy* **2013**, *127*, 100–108.

(53) Zhang, D.; Jin, C.; Tian, H.; Xiong, Y.; Zhang, H.; Qiao, P.; Fan, J.; Zhang, Z.; Li, Z. Y.; Li, J. An In Situ TEM Study of the Surface Oxidation of Palladium Nanocrystals Assisted by Electron Irradiation. *Nanoscale* **2017**, *9*, 6327–6333.

(54) Cazaux, J. Correlations between Ionization Radiation Effects in Transmission Electron. *Ultramicroscopy* **1995**, *60*, 41–425.

(55) Itikawa, Y. Cross Sections for Electron Collisions with Oxygen Molecules. *J. Phys. Chem. Ref. Data* **2009**, *38*, 1–20.

(56) Collot, P.; Gautherin, G.; Agius, B.; Rigo, S.; Rochet, F. Low-Pressure Oxidation of Silicon Stimulated by Low-Energy Electron Bombardment. *Philos. Mag. Part B* **1985**, *52*, 1051–1069.

(57) Knotek, M. L.; Feibelman, P. J. Ion Desorption by Core-Hole Auger Decay. *Phys. Rev. Lett.* **1978**, *40*, 964–967.

(58) Woll, C. The Chemistry and Physics of Zinc Oxide Surfaces. *Prog. Surf. Sci.* **2007**, *82*, 55–120.

(59) Ertl, G.; Neumann, M.; Streit, K. M. Chemisorption of CO on the Pt(111) Surface. *Surf. Sci.* **1977**, *64*, 393–410.

(60) Editor; H.P. Bonzel. Landolt-Börnstein Numerical Data and Functional Relationships in Science and Technology New Series / Editor in Chief: W. Martienssen Group III: Condensed Matter Volume 42 Physics of Covered Solid Surfaces Subvolume A Adsorbed Layers on Surfaces Part 4 Ads.

(61) Montano, M.; Bratlie, K.; Salmeron, M.; Somorjai, G. A. Hydrogen and Deuterium

Exchange on Pt(111) and Its Poisoning by Carbon Monoxide Studied by Surface Sensitive High-Pressure Techniques. *J. Am. Chem. Soc.* **2006**, *128*, 13229–13234.

(62) Liu, J. F.; Bei, Y. Y.; Wu, H. P.; Shen, D.; Gong, J. Z.; Li, X. G.; Wang, Y. W.; Jiang, N. P.; Jiang, J. Z. Synthesis of Relatively Monodisperse ZnO Nanocrystals from a Precursor Zinc 2,4-Pentanedionate. *Mater. Lett.* **2007**, *61*, 2837–2840.

(63) Demortière, A.; Petit, C. First Synthesis by Liquid-Liquid Phase Transfer of Magnetic Co XPt100-x Nanoalloys. *Langmuir* **2007**, *23*, 8575–8584.

(64) Giorgio, S.; Sao Joao, S.; Nitsche, S.; Chaudanson, D.; Sitja, G.; Henry, C. R. Environmental Electron Microscopy (ETEM) for Catalysts with a Closed E-Cell with Carbon Windows. *Ultramicroscopy* **2006**, *106*, 503–507.

(65) Alexander V. Naumkin, Anna Kraut-Vass, Stephen W. Gaarenstroom, and C. J. P. NIST X-ray Photoelectron Spectroscopy Database.